Quadridirectional eigenmode expansion scheme for 2-D modeling of wave propagation in integrated optics

*Manfred Hammer**

MESA$^+$ Research Institute, University of Twente, Enschede, The Netherlands

Abstract: The propagation of guided and nonconfined optical waves at fixed frequency through dielectric structures with piecewise constant, rectangular permittivity is considered in two spatial dimensions. Bidirectional versions of eigenmodes, computed for sequences of multilayer slab waveguides, constitute the expansion basis for the optical electromagnetic field. Dirichlet boundary conditions are sufficient to discretize the mode sets. Superpositions of two such expansions (bidirectional eigenmode propagation (BEP) fields), oriented along the two perpendicular coordinate axes, establish rigorous semianalytical solutions of the relevant Helmholtz wave equation on an unbounded, cross-shaped computational domain. The overlap of the lateral windows of the two BEP sets can be viewed as a rectangular computational window with fully transparent boundaries. Simulation results for a series of model systems (Gaussian beams in free space, Bragg gratings, waveguide crossings, a square cavity with perpendicular ports, and a 90° bend in a photonic crystal waveguide) illustrate the performance of the approach.

Keywords: waveguide optics, numerical modeling, eigenmode propagation techniques, omnidirectional light propagation, Helmholtz problems

PACS codes: 42.82.–m 42.82.Et

1 Introduction

With their potential for high integration densities, devices based on optical microcavities [1] or on photonic crystals [2] attract considerable attention in photonics research at present. Specific obstacles for the modeling originate from the high permittivity contrasts which are exploited for effective guiding and trapping of light waves: Phenomena like wide angle propagation and pronounced reflections are essential for the interference effects that the new structures rely upon.

Among the current simulation tools for scattering problems in integrated optics, the popular beam propagation methods [3] are not applicable at all, due to the underlying approximations. Concerning rigorous numerical simulations based on spatial discretizations, finite-difference-time-domain (FDTD) simulations [4] are the most common choice (frequency domain programs (Helmholtz-solvers) [5] exist as well, but receive much less attention). Unfortunately these fully general, finite-difference or finite-element based schemes are usually quite expensive in terms of computational effort, even in a 2D setting.

Where applicable, rigorous semi-analytic simulation tools, the class of bidirectional eigenmode propagation (BEP) or mode expansion techniques [6, 7, 8], can frequently offer a robust, accurate, and quite effective alternative. Packages with academic [9] and commercial backgrounds [10, 11] are available; the formalism in this paper is based on an own implementation as described in [12, 13]. For simulations in the optical regime, the BEP algorithms are so far set up exclusively along one major axis of light propagation. This viewpoint is decidedly inadequate for the high contrast structures, where one would expect that a rigorous (2D) simulation treats both relevant coordinate axes exactly alike. The approach outlined in this paper realizes that requirement, basically by means of superposition of eigenmode expansions along the two perpendicular axes.

Section 2 starts with a specification of the problem setting. Basis fields for the mode expansion and the related mode products (overlap integrals) are introduced in Section 2.1. Here one can restrict to eigenmodes of multilayer slab segments on finite cross section intervals with simple Dirichlet boundary conditions. In contrast to the complex modes defined by perfectly matched layers (PMLs) [14], that are necessary in conventional BEP schemes to realize transparent boundaries, the basis functions used here satisfy simple, well established orthogonality properties. At least for the present lossless structures, the mode profiles are real; propagation constants are to be searched on the real axis, not in the complex plane. The more or less standard spectral discretization procedure can be implemented in a quite robust and efficient way.

* *Department of Applied Mathematics, University of Twente P.O. Box 217, 7500 AE Enschede, The Netherlands*
Phone: +31/53/489-3448 Fax: +31/53/489-4833 E-mail: m.hammer@math.utwente.nl

The ansatz for the optical field is the subject of Section 2.2. By suitable projection on the basis elements the problem is reduced to a set of linear equations. Section 2.3 outlines this projection procedure together with our strategy to solve the problem for the coefficients in the mode expansion. Modes propagating in positive and negative direction along two coordinate axes play a role in this approach, hence this could be called a "quadridirectional eigenmode propagation" (QUEP) method. Section 3 summarizes the outcome of calculations for several (benchmark) structures of current interest.

Necessarily, with the Helmholtz wave equation being considered on a cross shaped domain limited by Dirichlet boundary conditions (perfectly conducting walls), the simulation setup resembles a crossing of hollow metal microwave waveguides, for which similar modeling approaches have been formulated. General formulations involving analytic expansions for different types of relatively simple microwave structures have been given e.g. in Refs. [15, 16, 17, 18]; similar lines of reasoning have been followed in the framework of the method of lines [19, 20, 21, 22, 23, 24]. However, here we are interested in regimes of simulation parameters where one can entirely disregard any influences of the enclosing walls. The focus is on the field in the region around the optical device, given as a refractive index inhomogeneity at the center of the domain, and around the connecting dielectric optical waveguides, that extend along the half-infinite ends of the cross.

2 Quadridirectional eigenmode expansion

The propagation of continuous optical electromagnetic waves in linear isotropic dielectric structures is to be simulated. The vacuum wavelength $\lambda = 2\pi/k = 2\pi \mathrm{c}/\omega$ specifies the fixed angular frequency ω corresponding to a time dependence $\sim \exp(\mathrm{i}\omega t)$ of all fields, for vacuum wavenumber k and vacuum speed of light c. For a description in two spatial dimensions, we choose a Cartesian coordinate system with relevant directions x (vertical) and z (horizontal), where all fields and the optical permittivity are assumed to be constant along the y-axis. The structure under investigation is given by a piecewise constant, rectangular refractive index profile, with the dielectric interfaces being parallel to either the x or z-axis. We restrict to lossless structures; all refractive index values are real.

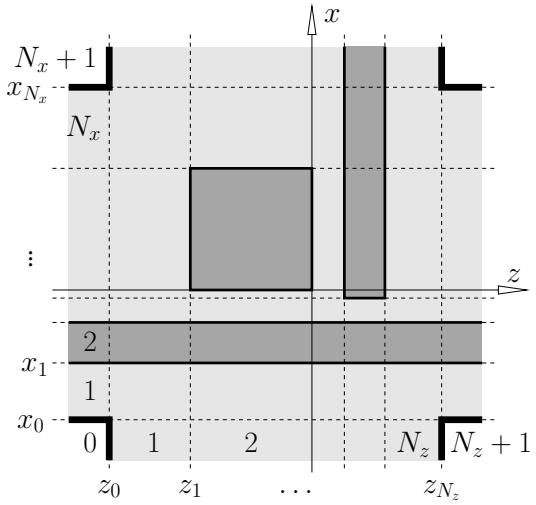

Figure 1: Rectangular decomposition of the computational domain. Horizontal interfaces at x_l, $l = 0, \ldots, N_x$ and vertical interfaces at z_s, $s = 0, \ldots, N_z$ divide the interesting inner region $(x, z) \in [x_0, x_{N_x}] \times [z_0, z_{N_z}]$ into N_x horizontal inner layers and N_z vertical inner slices. The outer regions with layer indices 0 and $N_x + 1$ and slice indices 0 and $N_z + 1$ are outwards unbounded.

Interest is in what happens inside a rectangular computational window $[x_0, x_{N_x}] \times [z_0, z_{N_z}]$. Figure 1 sketches the division of the domain into a number of vertical slices and horizontal layers. Here two viewpoints are possible: What follows can be regarded as an approach to solve the wave propagation problem on the rectangular inner domain, enclosed by four boundaries at $x = x_0, x_{N_x}$ and $z = z_0, z_{N_z}$ that are transparent for outgoing waves and that allow a specification of incoming fields. Alternatively, one can view this as a method to approximate a solution of the wave equation on an unbounded domain, consisting of the inner rectangle and the outwards unbounded external layers and slices. Both equivalent viewpoints are occasionally referred to in the following discussion.

The spectral discretization of the optical field is enforced by prescribing Dirichlet boundary conditions on the external border lines $z = z_0, z_{N_z}$, $x < x_0$ or $x > x_{N_x}$ and $x = x_0, x_{N_x}$, $z < z_0$ or $z > z_{N_z}$. One has to restrict the simulations to configurations, for which the assumption of vanishing basis fields on these lines is reasonable. The next section states the discretization more precisely.

2.1 Basis fields & mode products

For the present 2D structures made of isotropic materials, the optical electromagnetic field splits into TE and TM polarized parts. Due to the linearity of the problem, both parts can be treated separately (and the solutions later superimposed, where necessary). The formulation below applies simultaneously to TE and TM polarized fields.

We first focus on the decomposition into vertical slices, which represent the waveguide segments in a conventional bidirectional eigenmode propagation algorithm. Within slice number s, the region $(x, z) \in [x_0, x_{N_x}] \times [z_{s-1}, z_s]$, the refractive index is constant along z, but x-dependent (piecewise constant). We choose the eigenmodes associated with the multilayer slab profile of the slice as elements for the field expansion in Section 2.2, where the mode spectrum is discretized by Dirichlet boundary conditions, i.e. the basic components E_y (TE) or H_y (TM) of the mode profiles are assumed to vanish at $x = x_0$ and $x = x_{N_x}$, as well as outside that interval.

Propagating and evanescent modes up to a certain order $M_s^x - 1$ are included in the expansions. We apply a notation close to that introduced in Ref. [12]. Profile symbols $\boldsymbol{\psi}_{sm}^d = (E_{sm,x}^d, E_{sm,y}^d, E_{sm,z}^d, H_{sm,x}^d, H_{sm,y}^d, H_{sm,z}^d)$ collect the six electric and magnetic components of mode number m on slice s, the profile components are in general complex valued functions of x, such that for the present lossless problems each component is either purely real or purely imaginary. Modes that travel in the positive (forwards) and negative z-direction (backwards) are identified by symbols $d = \mathrm{f}$ and $d = \mathrm{b}$. With each basis field a propagation constant β_{sm} (real for propagating fields, purely imaginary for evanescent modes) is associated, such that $\beta > 0$ ($\beta < 0$) for a forwards (backwards) traveling propagating mode, or $-\mathrm{i}\beta < 0$ ($-\mathrm{i}\beta > 0$) for a forwards (backwards) traveling evanescent mode.

For purposes of field projection and power summation, we employ the following product of two general electromagnetic fields $\boldsymbol{\psi}_1 = (\boldsymbol{E}_1; \boldsymbol{H}_1)$ and $\boldsymbol{\psi}_2 = (\boldsymbol{E}_2; \boldsymbol{H}_2)$:

$$\left(\boldsymbol{\psi}_1; \boldsymbol{\psi}_2\right)_{[x_a, x_b]}^z = \frac{1}{4} \int_{x_a}^{x_b} (E_{1,x}^* H_{2,y} - E_{1,y}^* H_{2,x} + H_{1,y}^* E_{2,x} - H_{1,x}^* E_{2,y})(x, z)\, \mathrm{d}x\,. \tag{1}$$

Here the asterisk denotes complex conjugation. The notation is meant to be stretched as required, e.g. the z-position is omitted in case the expression is applied to two only x-dependent mode profiles. With the same field substituted for both arguments, the product (1) computes the z-component of the time averaged Poynting vector of that field. Assuming that equivalent profiles are employed for the directional mode variants, the power associated with each individual mode profile, used for purposes of normalization, reads $P_{sm} = \left|\left(\boldsymbol{\psi}_{sm}^{\mathrm{f}}; \boldsymbol{\psi}_{sm}^{\mathrm{f}}\right)_{[x_0, x_{N_x}]}\right|$, if mode m is propagating, and $P_{sm} = \left|\left(\boldsymbol{\psi}_{sm}^{\mathrm{f}}; \boldsymbol{\psi}_{sm}^{\mathrm{b}}\right)_{[x_0, x_{N_x}]}\right|$ in case mode m is evanescent. See Ref. [12] for the orthogonality properties of the basis mode sets, expressed by the product (1).

Upon viewing the structure alternatively as a stack of layers, an analogous spectral discretization procedure can be applied. Layer l comprises the region $(x, z) \in [x_{l-1}, x_l] \times [z_0, z_{N_z}]$; within each layer, the refractive index is constant along the x-direction. The eigenmodes associated with these layers, now discretized by Dirichlet boundary conditions at $z = z_0$ and $z = z_{N_z}$, constitute a second set of basis elements for the total field expansion.

We use a hat accent to mark quantities that are related to the wave propagation along the vertical axis. Accordingly, the profile symbol of mode m on layer l, that travels upwards in the positive x-direction $d = \mathrm{u}$ or downwards in the negative x-direction $d = \mathrm{d}$, reads $\hat{\boldsymbol{\psi}}_{lm}^d = (E_{lm,x}^d, E_{lm,y}^d, E_{lm,z}^d, H_{lm,x}^d, H_{lm,y}^d, H_{lm,z}^d)$. Each profile is accompanied by a propagation constant $\hat{\beta}_{lm}$, with the sign convention as introduced above. Per layer and direction of propagation, M_l^z modes up to order $M_l^z - 1$ are included in the expansions.

Analogously to Eq. (1), a product meant for fields $\hat{\boldsymbol{\psi}}_1 = (\boldsymbol{E}_1; \boldsymbol{H}_1)$ and $\hat{\boldsymbol{\psi}}_2 = (\boldsymbol{E}_2; \boldsymbol{H}_2)$ that travel along the x-axis can be introduced, now with an integration along a horizontal line:

$$\left\langle \hat{\boldsymbol{\psi}}_1; \hat{\boldsymbol{\psi}}_2 \right\rangle_{[z_a, z_b]}^x = \frac{1}{4} \int_{z_a}^{z_b} (E_{1,y}^* H_{2,z} - E_{1,z}^* H_{2,y} + H_{1,z}^* E_{2,y} - H_{1,y}^* E_{2,z})(x, z)\, \mathrm{d}z\,; \tag{2}$$

the power associated with the individual vertical mode profiles is expressed as $\hat{P}_{lm} = \left|\left\langle \hat{\boldsymbol{\psi}}_{lm}^{\mathrm{u}}; \hat{\boldsymbol{\psi}}_{lm}^{\mathrm{u}} \right\rangle_{[z_0, z_{N_z}]}\right|$, if mode m is propagating, and $\hat{P}_{lm} = \left|\left\langle \hat{\boldsymbol{\psi}}_{lm}^{\mathrm{u}}; \hat{\boldsymbol{\psi}}_{lm}^{\mathrm{d}} \right\rangle_{[z_0, z_{N_z}]}\right|$ in case mode m is evanescent.

Note that the formulation is somewhat redundant. Assuming that a horizontally traveling mode with profile $\boldsymbol{\psi}(x) = (E_x, E_y, E_z, H_x, H_y, H_z)(x)$ and propagation constant β has been calculated, for a local refractive index profile $n(x)$ on an interval $x \in [a, b]$. Then the same function n, now thought as being rotated by 90° and viewed as the refractive index profile $n(z)$ of a layer, supports a vertically traveling mode with profile $\hat{\boldsymbol{\psi}}(z) = (-E_z, E_y, -E_x, -H_z, H_y, -H_x)(z)$ and propagation constant $\hat{\beta} = \beta$ on an interval $z \in [a, b]$. Hence the entire set of basis modes can be represented by a uniform data structure.

2.2 Field ansatz

Using the symbols as introduced above and common complex notation, we write the following ansatz for the optical field in the overlap region of slice s and layer l:

$$\begin{aligned}
\begin{pmatrix} \boldsymbol{\mathcal{E}} \\ \boldsymbol{\mathcal{H}} \end{pmatrix}(x,z,t) &= \sum_{m=0}^{M_s^x-1} F_{sm} \frac{1}{\sqrt{P_{sm}}} \boldsymbol{\psi}_{sm}^{\mathrm{f}}(x)\, \mathrm{e}^{\mathrm{i}\omega t - \mathrm{i}\beta_{sm}(z - z_{s-1})} \\
&+ \sum_{m=0}^{M_s^x-1} B_{sm} \frac{1}{\sqrt{P_{sm}}} \boldsymbol{\psi}_{sm}^{\mathrm{b}}(x)\, \mathrm{e}^{\mathrm{i}\omega t + \mathrm{i}\beta_{sm}(z - z_{s})} \\
&+ \sum_{m=0}^{M_l^z-1} U_{lm} \frac{1}{\sqrt{\hat{P}_{lm}}} \hat{\boldsymbol{\psi}}_{lm}^{\mathrm{u}}(z)\, \mathrm{e}^{\mathrm{i}\omega t - \mathrm{i}\hat{\beta}_{lm}(x - x_{l-1})} \\
&+ \sum_{m=0}^{M_l^z-1} D_{lm} \frac{1}{\sqrt{\hat{P}_{lm}}} \hat{\boldsymbol{\psi}}_{lm}^{\mathrm{d}}(z)\, \mathrm{e}^{\mathrm{i}\omega t + \mathrm{i}\hat{\beta}_{lm}(x - x_{l})},
\end{aligned} \tag{3}$$

valid for $z_{s-1} < z < z_s,\ s = 1, \ldots, N_z$, and $x_{l-1} < x < x_l$, $l = 1, \ldots, N_x$. Note that the coefficients F_{sm} and B_{sm} of the forward and backward versions of mode m on slice s are relevant for all layers $l = 1, \ldots, N_x$. Likewise, the coefficients U_{lm} and D_{lm} of the upward and downward versions of mode m on layer l contribute to the field on all slices $s = 1, \ldots, N_z$.

A similar ansatz is used for the outer regions, where only modes traveling along the respective coordinate axes are present. The field in the half-infinite slices $s = 0$ and $s = N_z + 1$ only consists of forward and backward modes with coefficients F_{0m}, B_{0m}, $F_{N_z+1\,m}$, $B_{N_z+1\,m}$. On the half-infinite layers $l = 0$ and $l = N_x + 1$, the field is expanded solely into vertical, upwards and downwards traveling modes with coefficients U_{0m}, D_{0m}, $U_{N_x+1\,m}$, $D_{N_x+1\,m}$. For the external regions the coordinate offsets in the exponentials are obsolete and formally interpreted as $z_{-1} = z_0,\ z_{N_z+1} = z_{N_z},\ x_{-1} = x_0,\ x_{N_x+1} = x_{N_x}$.

A given scattering problem prescribes the coefficients F_{0m}, $B_{N_z+1\,m}$, U_{0m}, $D_{N_x+1\,m}$ of the incoming waves. For a problem with guided wave input, typically only a few (or only one) of these amplitudes are nonzero, which correspond to the approximations (Dirichlet boundary conditions) of the physically unbounded input modes. A more general exciting field profile is to be expanded into the basis mode set on the respective slices or layers, where for a physically relevant solution only propagating (i.e. non evanescent) modes contribute. One is interested in all remaining coefficients, in particular in the amplitudes of the outgoing waves B_{0m}, $F_{N_z+1\,m}$, D_{0m}, $U_{N_x+1\,m}$.

With the above mode normalization, orthogonality of the basis fields with respect to the products (1) and (2) allows to write the total optical power that is sent into the structure as the sum of the squared input amplitudes:

$$P_{\text{in}} = \sum_{m,\text{propag.}} |F_{0m}|^2 + \sum_{m,\text{propag.}} |B_{N_z+1\,m}|^2 + \sum_{m,\text{propag.}} |U_{0m}|^2 + \sum_{m,\text{propag.}} |D_{N_x+1\,m}|^2. \tag{4}$$

Analogously, the total scattered, outgoing optical power reads

$$P_{\text{out}} = \sum_{m,\text{propag.}} |B_{0m}|^2 + \sum_{m,\text{propag.}} |F_{N_z+1\,m}|^2 + \sum_{m,\text{propag.}} |D_{0m}|^2 + \sum_{m,\text{propag.}} |U_{N_x+1\,m}|^2. \tag{5}$$

Energy conservation requires that these quantities coincide (there are no evanescent waves in the incoming fields, hence the evanescent modes do not contribute to the power balance [12]). If external waveguide cores

are present, one is usually interested in the guided part of the outwards scattered power. The sum in Eq. (5) is then to be restricted to the coefficients of the interesting confined modes.

Now it is convenient to combine the previous coefficients and the mode normalization factors into dimensionless mode amplitudes $f_{sm} = F_{sm}/P_{sm}^{1/2}$, $b_{sm} = B_{sm}/P_{sm}^{1/2}$, $u_{lm} = U_{lm}/\hat{P}_{lm}^{1/2}$, $d_{lm} = D_{lm}/\hat{P}_{lm}^{1/2}$. For a more compact notation, these are merged into amplitude vectors $\boldsymbol{f}_s = (f_{sm})$, $\boldsymbol{b}_s = (b_{sm})$, $\boldsymbol{u}_l = (u_{lm})$, $\boldsymbol{d}_l = (d_{lm})$.

2.3 Algebraic procedure

Assuming that the basis modes are properly constructed, the superposition (3) satisfies the Maxwell equations exactly in all points of the computational domain, with the exception of the slice and layer interfaces. The coefficients of the expansion are to be determined such that across the interfaces the tangential components of the total electric and magnetic field are continuous. Via the curl-equations, this implies suitable continuity or discontinuity of the normal components of $\boldsymbol{\mathcal{E}}$ and $\boldsymbol{\mathcal{H}}$.

2.3.1 Horizontal bidirectional eigenmode expansion

Consider an inner vertical interface first, that separates slices s and $s+1$. The field expansions related to the adjacent slices are evaluated at the interface position $z = z_s$, and formally equated. The equation should include only the tangential components $\mathcal{E}_x$, $\mathcal{E}_y$, $\mathcal{H}_x$, $\mathcal{H}_y$; only these are relevant for the product (1). Assuming exact profiles $\hat{\boldsymbol{\psi}}_{lm}^{d}(z)$ of the vertically traveling modes, the contributions from these basis fields to the equation cancel in case of an inner interface with index $s \in \{1, \ldots, N_z - 1\}$.

To extract algebraic relations between the involved coefficients, the equation is projected onto the basis modes of the two slices by applying the products $\left(\boldsymbol{\psi}_{sn}^{d};\, .\,\right)_{[x_0, x_{N_x}]}$ and $\left(\boldsymbol{\psi}_{s+1\,n}^{d};\, .\,\right)_{[x_0, x_{N_x}]}$. In the first case one obtains the following set of equations, written directly in matrix form:

$$\mathsf{D}_{df}^{s}\mathsf{T}^{s}\boldsymbol{f}_s + \mathsf{D}_{d\mathrm{b}}^{s}\boldsymbol{b}_s = (\mathsf{O}_{\mathrm{f}d}^{s})^{*}\boldsymbol{f}_{s+1} + (\mathsf{O}_{\mathrm{b}d}^{s})^{*}\mathsf{T}^{s+1}\boldsymbol{b}_{s+1}\,, \quad \text{for} \quad d = \mathrm{f}, \mathrm{b}, \tag{6}$$

where the asterisk denotes the adjoint. The elements of the directional overlap matrices are given by

$$(\mathsf{D}_{dr}^{s})_{nm} = \left(\boldsymbol{\psi}_{sn}^{d}; \boldsymbol{\psi}_{sm}^{r}\right)_{[x_0, x_{N_x}]} \quad \text{and} \quad (\mathsf{O}_{dr}^{s})_{nm} = \left(\boldsymbol{\psi}_{s+1\,n}^{d}; \boldsymbol{\psi}_{sm}^{r}\right)_{[x_0, x_{N_x}]}. \tag{7}$$

The diagonal matrices D_{dr}^{s} contain the orthogonality properties of the basis modes [12] on a specific slice. Overlaps between the mode profiles of different slices are stored in the operators O_{dr}^{s}. The diagonal transfer matrices

$$(\mathsf{T}^{s})_{nm} = \mathrm{e}^{-\mathrm{i}\beta_{sm}(z_s - z_{s-1})}\delta_{nm}, \tag{8}$$

represent the exponential dependence of the modal solutions on the propagation coordinate, here the z-axis, with $\delta_{nm} = 1$ if $n = m$, and $\delta_{nm} = 0$ otherwise.

Likewise, the projection onto the basis fields of slice $s+1$ yields the equation

$$\mathsf{O}_{df}^{s}\mathsf{T}^{s}\boldsymbol{f}_s, + \mathsf{O}_{d\mathrm{b}}^{s}\boldsymbol{b}_s = \mathsf{D}_{df}^{s+1}\boldsymbol{f}_{s+1} + \mathsf{D}_{d\mathrm{b}}^{s+1}\mathsf{T}^{s+1}\boldsymbol{b}_{s+1}\,, \quad \text{for} \quad d = \mathrm{f}, \mathrm{b}. \tag{9}$$

By using the overlap matrices as defined in (7) as sub-matrices for the larger aggregates

$$\mathsf{D}^{s} = \begin{pmatrix} \mathsf{D}_{\mathrm{ff}}^{s} & \mathsf{D}_{\mathrm{fb}}^{s} \\ \mathsf{D}_{\mathrm{bf}}^{s} & \mathsf{D}_{\mathrm{bb}}^{s} \end{pmatrix}, \qquad \mathsf{O}^{s} = \begin{pmatrix} \mathsf{O}_{\mathrm{ff}}^{s} & \mathsf{O}_{\mathrm{fb}}^{s} \\ \mathsf{O}_{\mathrm{bf}}^{s} & \mathsf{O}_{\mathrm{bb}}^{s} \end{pmatrix}, \tag{10}$$

and by combining these into the operators

$$\mathsf{M}^{s,-} = (\mathsf{D}^{s})^{-1}(\mathsf{O}^{s})^{*}, \qquad \mathsf{M}^{s,+} = (\mathsf{D}^{s+1})^{-1}\mathsf{O}^{s}, \qquad \mathsf{M}^{s,\pm} = \begin{pmatrix} \mathsf{M}_{\mathrm{ff}}^{s,\pm} & \mathsf{M}_{\mathrm{fb}}^{s,\pm} \\ \mathsf{M}_{\mathrm{bf}}^{s,\pm} & \mathsf{M}_{\mathrm{bb}}^{s,\pm} \end{pmatrix}, \tag{11}$$

Eqs. (6), (9) can be given the more compact form:

$$\bullet\ \begin{pmatrix} \mathsf{T}^s \boldsymbol{f}_s \\ \boldsymbol{b}_s \end{pmatrix} = \begin{pmatrix} \mathsf{M}^{s,-}_{\mathrm{ff}} & \mathsf{M}^{s,-}_{\mathrm{fb}} \\ \mathsf{M}^{s,-}_{\mathrm{bf}} & \mathsf{M}^{s,-}_{\mathrm{bb}} \end{pmatrix} \begin{pmatrix} \boldsymbol{f}_{s+1} \\ \mathsf{T}^{s+1} \boldsymbol{b}_{s+1} \end{pmatrix}, \qquad \bullet\ \begin{pmatrix} \boldsymbol{f}_{s+1} \\ \mathsf{T}^{s+1} \boldsymbol{b}_{s+1} \end{pmatrix} = \begin{pmatrix} \mathsf{M}^{s,+}_{\mathrm{ff}} & \mathsf{M}^{s,+}_{\mathrm{fb}} \\ \mathsf{M}^{s,+}_{\mathrm{bf}} & \mathsf{M}^{s,+}_{\mathrm{bb}} \end{pmatrix} \begin{pmatrix} \mathsf{T}^s \boldsymbol{f}_s \\ \boldsymbol{b}_s \end{pmatrix}. \tag{12}$$

Assume for the moment that only the system (12) determines what happens around the junction at $z = z_s$. Then $\boldsymbol{f}_s$ and $\boldsymbol{b}_{s+1}$ must be regarded as given coefficients of incident waves; the junction scattering problem is to be solved for the coefficients $\boldsymbol{f}_{s+1}$ and $\boldsymbol{b}_s$ of the outgoing waves. One observes that the system (12) is twofold overdetermined.

In the limit of an infinite number of terms, the modal basis functions used for the field expansions represent complete sets of functions on the interval $[x_0, x_{N_x}]$. Hence, in this limit, the formal equality of fields that after projection leads to Eqs. (6), (9), becomes exact; correspondingly Eqs. (6), (9) and likewise the first and second part of Eq. (12) become equivalent.

The numerical implementation, however, requires a restriction to a finite, sufficiently large number of expansion terms, where one can expect that the former statements are still approximately satisfied. To proceed, a subset of the system (12) needs to be selected. We choose the sub-equations indicated by the symbols • in Eq. (12), for the following reasons. Based on this choice, the algorithm as outlined below allows to avoid applying the inverses of the matrices T^s (which would include exponentials growing with the slice length, related to the presence of evanescent modes). The procedure is formally applicable to expansions with differing sizes M^x_s on each slice, and the algorithm is "as implicit as possible". Concerning the numbers of expansion terms and the extension of the slices and layers, the simulations appear to be unconditionally stable (cf. the corresponding remarks in Ref. [13]). Perhaps other choices are possible and useful; what follows is based on the two equations

$$\boldsymbol{b}_s = \mathsf{M}^{s,-}_{\mathrm{bf}} \boldsymbol{f}_{s+1} + \mathsf{M}^{s,-}_{\mathrm{bb}} \mathsf{T}^{s+1} \boldsymbol{b}_{s+1}\,, \qquad \boldsymbol{f}_{s+1} = \mathsf{M}^{s,+}_{\mathrm{ff}} \mathsf{T}^s \boldsymbol{f}_s + \mathsf{M}^{s,+}_{\mathrm{fb}} \boldsymbol{b}_s\,, \tag{13}$$

established for each inner vertical interface at $z = z_s,\ s = 1, \ldots, N_z - 1$.

Now Eqs. (13) are to be combined, with a twofold aim. For the subsequent connection with the fields on the outer slices and with the perpendicular field expansion, on the one hand one would like to relate the amplitudes on slice $s = 1$ to those on slice $s = N_z$. On the other hand, the amplitudes on the intermediate slices are to be expressed explicitly in terms of those on slices 1 and N_z.

As a fist step, Eqs. (13) are rearranged such that for each junction at $z = z_s$ the amplitudes of the "outgoing" waves are explicitly given in terms of the amplitudes of the "incident" waves. After computing

$$\begin{array}{ll} \mathsf{J}^s_{\mathrm{ff}} = (1 - \mathsf{M}^{s,+}_{\mathrm{fb}} \mathsf{M}^{s,-}_{\mathrm{bf}})^{-1} \mathsf{M}^{s,+}_{\mathrm{ff}}\,, & \mathsf{J}^s_{\mathrm{fb}} = (1 - \mathsf{M}^{s,+}_{\mathrm{fb}} \mathsf{M}^{s,-}_{\mathrm{bf}})^{-1} \mathsf{M}^{s,+}_{\mathrm{fb}} \mathsf{M}^{s,-}_{\mathrm{bb}}\,, \\ \mathsf{J}^s_{\mathrm{bf}} = (1 - \mathsf{M}^{s,-}_{\mathrm{bf}} \mathsf{M}^{s,+}_{\mathrm{fb}})^{-1} \mathsf{M}^{s,-}_{\mathrm{bf}} \mathsf{M}^{s,+}_{\mathrm{ff}}\,, & \mathsf{J}^s_{\mathrm{bb}} = (1 - \mathsf{M}^{s,-}_{\mathrm{bf}} \mathsf{M}^{s,+}_{\mathrm{fb}})^{-1} \mathsf{M}^{s,-}_{\mathrm{bb}}\,, \end{array} \tag{14}$$

this reads

$$\begin{array}{rcl} \boldsymbol{f}_{s+1} & = & \mathsf{J}^s_{\mathrm{ff}} \mathsf{T}^s \boldsymbol{f}_s + \mathsf{J}^s_{\mathrm{fb}} \mathsf{T}^{s+1} \boldsymbol{b}_{s+1}\,, \\ \boldsymbol{b}_s & = & \mathsf{J}^s_{\mathrm{bf}} \mathsf{T}^s \boldsymbol{f}_s + \mathsf{J}^s_{\mathrm{bb}} \mathsf{T}^{s+1} \boldsymbol{b}_{s+1}\,, \end{array} \qquad s = 1, \ldots, N_{z-1}\,. \tag{15}$$

Then iteratively matrices are assembled that cover a sequence of slices in the same way, i.e. that for the sequence of inner slices 2 to s relate the coefficients $\boldsymbol{b}_1$ and $\boldsymbol{f}_{s+1}$ of "outgoing" waves explicitly to the coefficients $\boldsymbol{f}_1$ and $\boldsymbol{b}_{s+1}$ of "incident" modes (obviously this is relevant only for $N_z \geq 2$):

$$\begin{array}{rcl} \boldsymbol{f}_{s+1} & = & \mathsf{K}^s_{\mathrm{ff}} \mathsf{T}^1 \boldsymbol{f}_1 + \mathsf{K}^s_{\mathrm{fb}} \mathsf{T}^{s+1} \boldsymbol{b}_{s+1}\,, \\ \boldsymbol{b}_1 & = & \mathsf{K}^s_{\mathrm{bf}} \mathsf{T}^1 \boldsymbol{f}_1 + \mathsf{K}^s_{\mathrm{bb}} \mathsf{T}^{s+1} \boldsymbol{b}_{s+1}\,, \end{array} \qquad s = 1, \ldots, N_{z-1}\,. \tag{16}$$

Starting with $\mathsf{K}^1_{dr} = \mathsf{J}^1_{dr}$ and using the intermediate quantities

$$\begin{array}{ll} \mathsf{A}^s_{\mathrm{ff}} = (1 - \mathsf{K}^s_{\mathrm{fb}} \mathsf{T}^{s+1} \mathsf{J}^{s+1}_{\mathrm{bf}} \mathsf{T}^{s+1})^{-1} \mathsf{K}^s_{\mathrm{ff}}, & \mathsf{A}^s_{\mathrm{fb}} = (1 - \mathsf{K}^s_{\mathrm{fb}} \mathsf{T}^{s+1} \mathsf{J}^{s+1}_{\mathrm{bf}} \mathsf{T}^{s+1})^{-1} \mathsf{K}^s_{\mathrm{fb}} \mathsf{T}^{s+1} \mathsf{J}^{s+1}_{\mathrm{bb}}, \\ \mathsf{A}^s_{\mathrm{bf}} = (1 - \mathsf{J}^{s+1}_{\mathrm{bf}} \mathsf{T}^{s+1} \mathsf{K}^s_{\mathrm{fb}} \mathsf{T}^{s+1})^{-1} \mathsf{J}^{s+1}_{\mathrm{bf}} \mathsf{T}^{s+1} \mathsf{K}^s_{\mathrm{ff}}, & \mathsf{A}^s_{\mathrm{bb}} = (1 - \mathsf{J}^{s+1}_{\mathrm{bf}} \mathsf{T}^{s+1} \mathsf{K}^s_{\mathrm{fb}} \mathsf{T}^{s+1})^{-1} \mathsf{J}^{s+1}_{\mathrm{bb}}, \end{array} \tag{17}$$

the matrices K_{dr}^{s} can be calculated along the recipe:

$$\begin{array}{ll} \mathsf{K}_{\mathrm{ff}}^{s+1} = \mathsf{J}_{\mathrm{ff}}^{s+1}\mathsf{T}^{s+1}\mathsf{A}_{\mathrm{ff}}^{s}\,, & \mathsf{K}_{\mathrm{fb}}^{s+1} = \mathsf{J}_{\mathrm{ff}}^{s+1}\mathsf{T}^{s+1}\mathsf{A}_{\mathrm{fb}}^{s} + \mathsf{J}_{\mathrm{fb}}^{s+1}\,, \\ \mathsf{K}_{\mathrm{bf}}^{s+1} = \mathsf{K}_{\mathrm{bf}}^{s} + \mathsf{K}_{\mathrm{bb}}^{s}\mathsf{T}^{s+1}\mathsf{A}_{\mathrm{bf}}^{s}\,, & \mathsf{K}_{\mathrm{bb}}^{s+1} = \mathsf{K}_{\mathrm{bb}}^{s}\mathsf{T}^{s+1}\mathsf{A}_{\mathrm{bb}}^{s}\,. \end{array} \tag{18}$$

After the final step, the matrices $\mathsf{K}_{dr}^{N_z-1}$ cover the entire inner sequence of slices, as required:

$$\begin{aligned} \boldsymbol{f}_{N_z} &= \mathsf{K}_{\mathrm{ff}}^{N_z-1}\mathsf{T}^{1}\boldsymbol{f}_1 + \mathsf{K}_{\mathrm{fb}}^{N_z-1}\mathsf{T}^{N_z}\boldsymbol{b}_{N_z}\,, \\ \boldsymbol{b}_1 &= \mathsf{K}_{\mathrm{bf}}^{N_z-1}\mathsf{T}^{1}\boldsymbol{f}_1 + \mathsf{K}_{\mathrm{bb}}^{N_z-1}\mathsf{T}^{N_z}\boldsymbol{b}_{N_z}\,. \end{aligned} \tag{19}$$

In a kind of backsubstitution process, the system is solved for the intermediate coefficients, given the amplitudes of the "incident" modes on the outer slices of the sequence (this is relevant only if $N_z \geq 3$). Starting with $\mathsf{S}_{dr}^{N_z-1} = \mathsf{A}_{dr}^{N_z-2}$, iteratively matrices S_{dr}^{s} are built according to the equations

$$\begin{array}{ll} \mathsf{S}_{\mathrm{ff}}^{s-1} = \mathsf{A}_{\mathrm{ff}}^{s-2} + \mathsf{A}_{\mathrm{fb}}^{s-2}\mathsf{T}^{s}\mathsf{S}_{\mathrm{bf}}^{s}\,, & \mathsf{S}_{\mathrm{fb}}^{s-1} = \mathsf{A}_{\mathrm{fb}}^{s-2}\mathsf{T}^{s}\mathsf{S}_{\mathrm{bb}}^{s}\,, \\ \mathsf{S}_{\mathrm{bf}}^{s-1} = \mathsf{A}_{\mathrm{bf}}^{s-2} + \mathsf{A}_{\mathrm{bb}}^{s-2}\mathsf{T}^{s}\mathsf{S}_{\mathrm{bf}}^{s}\,, & \mathsf{S}_{\mathrm{bb}}^{s-1} = \mathsf{A}_{\mathrm{bb}}^{s-2}\mathsf{T}^{s}\mathsf{S}_{\mathrm{bb}}^{s}\,, \end{array} \tag{20}$$

such that

$$\begin{aligned} \boldsymbol{f}_s &= \mathsf{S}_{\mathrm{ff}}^{s}\mathsf{T}^{1}\boldsymbol{f}_1 + \mathsf{S}_{\mathrm{fb}}^{s}\mathsf{T}^{N_z}\boldsymbol{b}_{N_z}\,, \\ \boldsymbol{b}_s &= \mathsf{S}_{\mathrm{bf}}^{s}\mathsf{T}^{1}\boldsymbol{f}_1 + \mathsf{S}_{\mathrm{bb}}^{s}\mathsf{T}^{N_z}\boldsymbol{b}_{N_z}\,. \end{aligned} \tag{21}$$

As an intermediate summary, these formulas allow to compute matrices $\mathsf{K}_{dr} = \mathsf{K}_{dr}^{N_z-1}$ and S_{dr}^{s} that connect all amplitudes of horizontally traveling modes on the inner slices in an explicit way:

$$\begin{pmatrix} \boldsymbol{f}_{N_z} \\ \boldsymbol{b}_1 \end{pmatrix} = \begin{pmatrix} \mathsf{K}_{\mathrm{ff}} & \mathsf{K}_{\mathrm{fb}} \\ \mathsf{K}_{\mathrm{bf}} & \mathsf{K}_{\mathrm{bb}} \end{pmatrix} \begin{pmatrix} \mathsf{T}^{1}\boldsymbol{f}_1 \\ \mathsf{T}^{N_z}\boldsymbol{b}_{N_z} \end{pmatrix}, \quad \begin{pmatrix} \boldsymbol{f}_s \\ \boldsymbol{b}_s \end{pmatrix} = \begin{pmatrix} \mathsf{S}_{\mathrm{ff}}^{s} & \mathsf{S}_{\mathrm{fb}}^{s} \\ \mathsf{S}_{\mathrm{bf}}^{s} & \mathsf{S}_{\mathrm{bb}}^{s} \end{pmatrix} \begin{pmatrix} \mathsf{T}^{1}\boldsymbol{f}_1 \\ \mathsf{T}^{N_z}\boldsymbol{b}_{N_z} \end{pmatrix}, \quad s = 2, \ldots, N_z - 1. \tag{22}$$

Basically, the preceding formalism represents a conventional BEP algorithm, though one that takes into account simultaneous influx from both ends of the slice sequence.

2.3.2 Vertical bidirectional eigenmode expansion

We now switch to a viewpoint, that considers the structure under investigation as a stack of layers, in place of the former sequence of slices. By substituting layers for slices, replacing the product (1) by (2), and applying projections onto the basis modes related to the decomposition into layers, connector matrices for the vertical wave propagation can be established in a precisely analogous way. The resulting relations read

$$\begin{pmatrix} \boldsymbol{u}_{N_x} \\ \boldsymbol{d}_1 \end{pmatrix} = \begin{pmatrix} \hat{\mathsf{K}}_{\mathrm{uu}} & \hat{\mathsf{K}}_{\mathrm{ud}} \\ \hat{\mathsf{K}}_{\mathrm{du}} & \hat{\mathsf{K}}_{\mathrm{dd}} \end{pmatrix} \begin{pmatrix} \hat{\mathsf{T}}^{1}\boldsymbol{u}_1 \\ \hat{\mathsf{T}}^{N_x}\boldsymbol{d}_{N_x} \end{pmatrix}, \quad \begin{pmatrix} \boldsymbol{u}_l \\ \boldsymbol{d}_l \end{pmatrix} = \begin{pmatrix} \hat{\mathsf{S}}_{\mathrm{uu}}^{l} & \hat{\mathsf{S}}_{\mathrm{ud}}^{l} \\ \hat{\mathsf{S}}_{\mathrm{du}}^{l} & \hat{\mathsf{S}}_{\mathrm{dd}}^{l} \end{pmatrix} \begin{pmatrix} \hat{\mathsf{T}}^{1}\boldsymbol{u}_1 \\ \hat{\mathsf{T}}^{N_x}\boldsymbol{d}_{N_x} \end{pmatrix}, \quad l = 2, \ldots, N_x - 1. \tag{23}$$

Here again the hat accent identifies the quantities related to the "vertical" BEP setting.

2.3.3 Combination of the horizontal and vertical expansions

It remains to look at the boundaries of the computational window, i.e. at the interfaces between the inner rectangle and the outer, half infinite slices or layers, respectively. This will lead to a connection of the two — so far independent — BEP representations for the interior.

We first focus on the left vertical boundary of the computational window. On slice 0 on the left of the junction at $z = z_0$, the field expansion consists of forwards and backwards traveling modes only, while in slice 1 on the right of the junction, the full expansion (3) applies. As before, the components $\mathcal{E}_x$, $\mathcal{E}_y$, $\mathcal{H}_x$, $\mathcal{H}_y$, evaluated at $z = z_0$, are equated. With the vertical mode profiles vanishing on the left of the junction, now the contributions of the upwards and downwards traveling basis fields do not cancel in these equations. We follow the procedure along Eqs. (6)–(13), where additional terms related to the coefficients $\boldsymbol{u}_l$ and $\boldsymbol{d}_l$ have to be taken into account.

The projection $\left(\boldsymbol{\psi}^d_{0n};\ .\ \right)^{z_0}_{[x_0,x_{N_x}]}$ of the equated expansions onto the basis profiles of the external slice 0 results in the equations

$$\mathsf{D}^0_{df}\boldsymbol{f}_0+\mathsf{D}^0_{d\mathrm{b}}\boldsymbol{b}_0=(\mathsf{O}^0_{\mathrm{f}d})^*\boldsymbol{f}_1+(\mathsf{O}^0_{\mathrm{b}d})^*\mathsf{T}^1\boldsymbol{b}_1+\sum_{l=1}^{N_x}\mathsf{C}^{0l\,z_0}_{d\mathrm{u}}\boldsymbol{u}_l+\sum_{l=1}^{N_x}\mathsf{C}^{0l\,z_0}_{d\mathrm{d}}\boldsymbol{d}_l\,,\quad\text{for}\quad d=\mathrm{f},\mathrm{b}. \tag{24}$$

Definitions (7) and (8) apply; additionally the cross-overlaps

$$(\mathsf{C}^{sl\,z}_{dr})_{nm}=\begin{cases}\left(\boldsymbol{\psi}^d_{sn};\hat{\boldsymbol{\psi}}^{\mathrm{u}}_{lm}(z)\,\mathrm{e}^{-\mathrm{i}\hat{\beta}_{lm}(x-x_{l-1})}\right)^z_{[x_{l-1},x_l]} & \text{for } r=\mathrm{u},\\ \left(\boldsymbol{\psi}^d_{sn};\hat{\boldsymbol{\psi}}^{\mathrm{d}}_{lm}(z)\,\mathrm{e}^{\mathrm{i}\hat{\beta}_{lm}(x-x_l)}\right)^z_{[x_{l-1},x_l]} & \text{for } r=\mathrm{d},\end{cases} \tag{25}$$

appear. Eqs. (23) can be used to eliminate the coefficients related to the internal layers. That leads to the simpler equations

$$\mathsf{D}^0_{df}\boldsymbol{f}_0+\mathsf{D}^0_{d\mathrm{b}}\boldsymbol{b}_0=(\mathsf{O}^0_{\mathrm{f}d})^*\boldsymbol{f}_1+(\mathsf{O}^0_{\mathrm{b}d})^*\mathsf{T}^1\boldsymbol{b}_1+\mathsf{V}^{0\,z_0}_{d\mathrm{u}}\boldsymbol{u}_1+\mathsf{V}^{0\,z_0}_{d\mathrm{d}}\boldsymbol{d}_{N_x}\,,\quad\text{for}\quad d=\mathrm{f},\mathrm{b}, \tag{26}$$

where the summations are now shifted to the matrices

$$\begin{aligned}\mathsf{V}^{s\,z}_{d\mathrm{u}}&=\sum_{l=2}^{N_x-1}\left(\mathsf{C}^{sl\,z}_{d\mathrm{u}}\hat{\mathsf{S}}^l_{\mathrm{uu}}+\mathsf{C}^{sl\,z}_{d\mathrm{d}}\hat{\mathsf{S}}^l_{\mathrm{du}}\right)\hat{\mathsf{T}}^1+\mathsf{C}^{s1\,z}_{d\mathrm{u}}+\mathsf{C}^{s\,N_x\,z}_{d\mathrm{u}}\hat{\mathsf{K}}_{\mathrm{uu}}\hat{\mathsf{T}}^1+\mathsf{C}^{s1\,z}_{d\mathrm{d}}\hat{\mathsf{K}}_{\mathrm{du}}\hat{\mathsf{T}}^1\,,\\ \mathsf{V}^{s\,z}_{d\mathrm{d}}&=\sum_{l=2}^{N_x-1}\left(\mathsf{C}^{sl\,z}_{d\mathrm{u}}\hat{\mathsf{S}}^l_{\mathrm{ud}}+\mathsf{C}^{sl\,z}_{d\mathrm{d}}\hat{\mathsf{S}}^l_{\mathrm{dd}}\right)\hat{\mathsf{T}}^{N_x}+\mathsf{C}^{s\,N_x\,z}_{d\mathrm{d}}+\mathsf{C}^{s\,N_x\,z}_{d\mathrm{u}}\hat{\mathsf{K}}_{\mathrm{ud}}\hat{\mathsf{T}}^{N_x}+\mathsf{C}^{s1\,z}_{d\mathrm{d}}\hat{\mathsf{K}}_{\mathrm{dd}}\hat{\mathsf{T}}^{N_x}\,.\end{aligned} \tag{27}$$

Likewise, the projection $\left(\boldsymbol{\psi}^d_{1n};\ .\ \right)^{z_0}_{[x_0,x_{N_x}]}$ onto the modes of slice 1 leads to the expressions

$$\mathsf{O}^0_{df}\boldsymbol{f}_0+\mathsf{O}^0_{d\mathrm{b}}\boldsymbol{b}_0=\mathsf{D}^1_{df}\boldsymbol{f}_1+\mathsf{D}^1_{d\mathrm{b}}\mathsf{T}^1\boldsymbol{b}_1+\mathsf{V}^{1\,z_0}_{d\mathrm{u}}\boldsymbol{u}_1+\mathsf{V}^{1\,z_0}_{d\mathrm{d}}\boldsymbol{d}_{N_x}\,,\quad\text{for}\quad d=\mathrm{f},\mathrm{b}. \tag{28}$$

Using the definitions (10), (11) and additionally

$$\mathsf{V}^{s\,z}=\begin{pmatrix}\mathsf{V}^{s\,z}_{\mathrm{fu}} & \mathsf{V}^{s\,z}_{\mathrm{fd}}\\ \mathsf{V}^{s\,z}_{\mathrm{bu}} & \mathsf{V}^{s\,z}_{\mathrm{bd}}\end{pmatrix},\quad \mathsf{R}^{0,-}=(\mathsf{D}^0)^{-1}\mathsf{V}^{0\,z_0},\quad \mathsf{R}^{0,+}=(\mathsf{D}^1)^{-1}\mathsf{V}^{1\,z_0},\quad \mathsf{R}^{0,\pm}=\begin{pmatrix}\mathsf{R}^{0,\pm}_{\mathrm{fu}} & \mathsf{R}^{0,\pm}_{\mathrm{fd}}\\ \mathsf{R}^{0,\pm}_{\mathrm{bu}} & \mathsf{R}^{0,\pm}_{\mathrm{bd}}\end{pmatrix}, \tag{29}$$

Eqs. (26), (28) can be given the form

$$\begin{aligned}&\bullet\ \begin{pmatrix}\boldsymbol{f}_0\\ \boldsymbol{b}_0\end{pmatrix}=\begin{pmatrix}\mathsf{M}^{0,-}_{\mathrm{ff}} & \mathsf{M}^{0,-}_{\mathrm{fb}}\\ \mathsf{M}^{0,-}_{\mathrm{bf}} & \mathsf{M}^{0,-}_{\mathrm{bb}}\end{pmatrix}\begin{pmatrix}\boldsymbol{f}_1\\ \mathsf{T}^1\boldsymbol{b}_1\end{pmatrix}+\begin{pmatrix}\mathsf{R}^{0,-}_{\mathrm{fu}} & \mathsf{R}^{0,-}_{\mathrm{ff}}\\ \mathsf{R}^{0,-}_{\mathrm{bu}} & \mathsf{R}^{0,-}_{\mathrm{bd}}\end{pmatrix}\begin{pmatrix}\boldsymbol{u}_1\\ \boldsymbol{d}_{N_x}\end{pmatrix},\\ &\bullet\ \begin{pmatrix}\boldsymbol{f}_1\\ \mathsf{T}^1\boldsymbol{b}_1\end{pmatrix}=\begin{pmatrix}\mathsf{M}^{0,+}_{\mathrm{ff}} & \mathsf{M}^{0,+}_{\mathrm{fb}}\\ \mathsf{M}^{0,+}_{\mathrm{bf}} & \mathsf{M}^{0,+}_{\mathrm{bb}}\end{pmatrix}\begin{pmatrix}\boldsymbol{f}_0\\ \boldsymbol{b}_0\end{pmatrix}-\begin{pmatrix}\mathsf{R}^{0,+}_{\mathrm{fu}} & \mathsf{R}^{0,+}_{\mathrm{ff}}\\ \mathsf{R}^{0,+}_{\mathrm{bu}} & \mathsf{R}^{0,+}_{\mathrm{bd}}\end{pmatrix}\begin{pmatrix}\boldsymbol{u}_1\\ \boldsymbol{d}_{N_x}\end{pmatrix}.\end{aligned} \tag{30}$$

As for the internal interfaces, the system (30) is twofold overdetermined; only the two rows marked by the symbol $\bullet$, i.e. only the equations

$$\begin{aligned}\boldsymbol{b}_0&=\mathsf{M}^{0,-}_{\mathrm{bf}}\boldsymbol{f}_1+\mathsf{M}^{0,-}_{\mathrm{bb}}\mathsf{T}^1\boldsymbol{b}_1+\mathsf{R}^{0,-}_{\mathrm{bu}}\boldsymbol{u}_1+\mathsf{R}^{0,-}_{\mathrm{bd}}\boldsymbol{d}_{N_x}\,,\\ \boldsymbol{f}_1&=\mathsf{M}^{0,+}_{\mathrm{ff}}\boldsymbol{f}_0+\mathsf{M}^{0,+}_{\mathrm{fb}}\boldsymbol{b}_0-\mathsf{R}^{0,+}_{\mathrm{fu}}\boldsymbol{u}_1-\mathsf{R}^{0,+}_{\mathrm{fd}}\boldsymbol{d}_{N_x}\end{aligned} \tag{31}$$

enter the further procedure.

Analogously, the remaining boundaries of the computational window can be handled. Using the definitions (10), (11), (27), and

$$\mathsf{R}^{N_z,-}=(\mathsf{D}^{N_z})^{-1}\mathsf{V}^{N_z\,z_{N_z}},\quad \mathsf{R}^{N_z,+}=(\mathsf{D}^{N_z+1})^{-1}\mathsf{V}^{N_z+1\,z_{N_z}},\quad \mathsf{R}^{N_z,\pm}=\begin{pmatrix}\mathsf{R}^{N_z,\pm}_{\mathrm{fu}} & \mathsf{R}^{N_z,\pm}_{\mathrm{fd}}\\ \mathsf{R}^{N_z,\pm}_{\mathrm{bu}} & \mathsf{R}^{N_z,\pm}_{\mathrm{bd}}\end{pmatrix}, \tag{32}$$

one obtains the equations

$$\begin{aligned} \boldsymbol{b}_{N_z} &= \mathsf{M}_{\mathrm{bf}}^{N_z,-}\boldsymbol{f}_{N_z+1} + \mathsf{M}_{\mathrm{bb}}^{N_z,-}\boldsymbol{b}_{N_z+1} - \mathsf{R}_{\mathrm{bu}}^{N_z,-}\boldsymbol{u}_1 - \mathsf{R}_{\mathrm{bd}}^{N_z,-}\boldsymbol{d}_{N_x}\,, \\ \boldsymbol{f}_{N_z+1} &= \mathsf{M}_{\mathrm{ff}}^{N_z,+}\mathsf{T}^{N_z}\boldsymbol{f}_{N_z} + \mathsf{M}_{\mathrm{fb}}^{N_z,+}\boldsymbol{b}_{N_z} + \mathsf{R}_{\mathrm{fu}}^{N_z,+}\boldsymbol{u}_1 + \mathsf{R}_{\mathrm{fd}}^{N_z,+}\boldsymbol{d}_{N_x} \end{aligned} \tag{33}$$

for the right, vertical boundary at $z = z_{N_z}$.

With the cross-overlaps on the upper and lower horizontal interfaces

$$(\hat{\mathsf{C}}_{dr}^{ls\,x})_{nm} = \begin{cases} \langle \hat{\boldsymbol{\psi}}_{ln}^{d}; \boldsymbol{\psi}_{sm}^{\mathrm{f}}(x)\, \mathrm{e}^{-\mathrm{i}\beta_{sm}(z-z_{s-1})}\rangle_{[z_{s-1},z_s]}^{x} & \text{for } r = \mathrm{f}, \\ \langle \hat{\boldsymbol{\psi}}_{ln}^{d}; \boldsymbol{\psi}_{sm}^{\mathrm{b}}(x)\, \mathrm{e}^{\mathrm{i}\beta_{sm}(z-z_{s})}\rangle_{[z_{s-1},z_s]}^{x} & \text{for } r = \mathrm{b}, \end{cases} \tag{34}$$

with the related matrices

$$\begin{aligned} \hat{\mathsf{V}}_{\mathrm{df}}^{l\,x} &= \sum_{s=2}^{N_z-1} \big(\hat{\mathsf{C}}_{\mathrm{df}}^{ls\,x}\mathsf{S}_{\mathrm{ff}}^{s} + \hat{\mathsf{C}}_{\mathrm{db}}^{ls\,x}\mathsf{S}_{\mathrm{bf}}^{s}\big)\mathsf{T}^{1} + \hat{\mathsf{C}}_{\mathrm{df}}^{l1\,x} + \hat{\mathsf{C}}_{\mathrm{df}}^{l\,N_z\,x}\mathsf{K}_{\mathrm{ff}}\mathsf{T}^{1} + \hat{\mathsf{C}}_{\mathrm{db}}^{l1\,x}\mathsf{K}_{\mathrm{bf}}\mathsf{T}^{1}\,, \\ \hat{\mathsf{V}}_{\mathrm{db}}^{l\,x} &= \sum_{s=2}^{N_z-1} \big(\hat{\mathsf{C}}_{\mathrm{df}}^{ls\,x}\mathsf{S}_{\mathrm{fb}}^{s} + \hat{\mathsf{C}}_{\mathrm{db}}^{ls\,x}\mathsf{S}_{\mathrm{bb}}^{s}\big)\mathsf{T}^{N_z} + \hat{\mathsf{C}}_{\mathrm{db}}^{l\,N_z\,x} + \hat{\mathsf{C}}_{\mathrm{df}}^{l\,N_z\,x}\mathsf{K}_{\mathrm{fb}}\mathsf{T}^{N_z} + \hat{\mathsf{C}}_{\mathrm{db}}^{s1\,x}\mathsf{K}_{\mathrm{bb}}\mathsf{T}^{N_z}\,, \end{aligned} \tag{35}$$

and assignments analogous to Eqs. (29), (32)

$$\hat{\mathsf{V}}^{l\,x} = \begin{pmatrix} \hat{\mathsf{V}}_{\mathrm{uf}}^{l\,x} & \hat{\mathsf{V}}_{\mathrm{ub}}^{l\,x} \\ \hat{\mathsf{V}}_{\mathrm{df}}^{l\,x} & \hat{\mathsf{V}}_{\mathrm{db}}^{l\,x} \end{pmatrix}, \quad \hat{\mathsf{R}}^{0,-} = (\hat{\mathsf{D}}^{0})^{-1}\hat{\mathsf{V}}^{0\,x_0}\,, \quad \hat{\mathsf{R}}^{0,+} = (\hat{\mathsf{D}}^{1})^{-1}\hat{\mathsf{V}}^{1\,x_0}\,, \quad \hat{\mathsf{R}}^{0,\pm} = \begin{pmatrix} \hat{\mathsf{R}}_{\mathrm{uf}}^{0,\pm} & \hat{\mathsf{R}}_{\mathrm{ub}}^{0,\pm} \\ \hat{\mathsf{R}}_{\mathrm{df}}^{0,\pm} & \hat{\mathsf{R}}_{\mathrm{db}}^{0,\pm} \end{pmatrix}, \tag{36}$$

$$\hat{\mathsf{R}}^{N_x,-} = (\hat{\mathsf{D}}^{N_x})^{-1}\hat{\mathsf{V}}^{N_x\,x_{N_x}}\,, \quad \hat{\mathsf{R}}^{N_x,+} = (\hat{\mathsf{D}}^{N_x+1})^{-1}\hat{\mathsf{V}}^{N_x+1\,x_{N_x}}\,, \quad \hat{\mathsf{R}}^{N_x,\pm} = \begin{pmatrix} \hat{\mathsf{R}}_{\mathrm{uf}}^{N_x,\pm} & \hat{\mathsf{R}}_{\mathrm{ub}}^{N_x,\pm} \\ \hat{\mathsf{R}}_{\mathrm{df}}^{N_x,\pm} & \hat{\mathsf{R}}_{\mathrm{db}}^{N_x,\pm} \end{pmatrix}, \tag{37}$$

one arrives at the equations

$$\begin{aligned} \boldsymbol{d}_0 &= \hat{\mathsf{M}}_{\mathrm{du}}^{0,-}\boldsymbol{u}_1 + \hat{\mathsf{M}}_{\mathrm{dd}}^{0,-}\hat{\mathsf{T}}^{1}\boldsymbol{d}_1 + \hat{\mathsf{R}}_{\mathrm{df}}^{0,-}\boldsymbol{f}_1 + \hat{\mathsf{R}}_{\mathrm{db}}^{0,-}\boldsymbol{b}_{N_z}\,, \\ \boldsymbol{u}_1 &= \hat{\mathsf{M}}_{\mathrm{uu}}^{0,+}\boldsymbol{u}_0 + \hat{\mathsf{M}}_{\mathrm{ud}}^{0,+}\boldsymbol{d}_0 - \hat{\mathsf{R}}_{\mathrm{uf}}^{0,+}\boldsymbol{f}_1 - \hat{\mathsf{R}}_{\mathrm{ub}}^{0,+}\boldsymbol{b}_{N_z} \end{aligned} \tag{38}$$

for the mode amplitudes around the horziontal interface at $x = x_0$, and

$$\begin{aligned} \boldsymbol{d}_{N_x} &= \hat{\mathsf{M}}_{\mathrm{du}}^{N_x,-}\boldsymbol{u}_{N_x+1} + \hat{\mathsf{M}}_{\mathrm{dd}}^{N_x,-}\boldsymbol{d}_{N_x+1} - \hat{\mathsf{R}}_{\mathrm{df}}^{N_x,-}\boldsymbol{f}_1 - \hat{\mathsf{R}}_{\mathrm{db}}^{N_x,-}\boldsymbol{b}_{N_z}\,, \\ \boldsymbol{u}_{N_x+1} &= \hat{\mathsf{M}}_{\mathrm{uu}}^{N_x,+}\hat{\mathsf{T}}^{N_x}\boldsymbol{u}_{N_x} + \hat{\mathsf{M}}_{\mathrm{ud}}^{N_x,+}\boldsymbol{d}_{N_x} + \hat{\mathsf{R}}_{\mathrm{uf}}^{N_x,+}\boldsymbol{f}_1 + \hat{\mathsf{R}}_{\mathrm{ub}}^{N_x,+}\boldsymbol{b}_{N_z} \end{aligned} \tag{39}$$

for the coefficients related to the interface at $x = x_{N_x}$.

Finally, one has to combine Eqs. (31), (33), (38), and (39). A possible solution procedure starts with eliminating the coefficients $\boldsymbol{f}_{N_z}$, $\boldsymbol{b}_1$, $\boldsymbol{u}_{N_x}$, $\boldsymbol{d}_1$, by using the first equalities of Eqs. (22), (23). This results in explicit dependences of the primary unknowns $\boldsymbol{b}_0$, $\boldsymbol{f}_{N_z+1}$, $\boldsymbol{d}_0$, $\boldsymbol{u}_{N_x+1}$ on the coefficients $\boldsymbol{f}_1$, $\boldsymbol{b}_{N_z}$, $\boldsymbol{u}_1$, $\boldsymbol{d}_{N_x}$ of the inwards traveling waves on the outermost slices and layers inside the computational window:

$$\begin{aligned} \boldsymbol{f}_{N_z+1} &= \mathsf{M}_{\mathrm{ff}}^{N_z,+}\mathsf{T}^{N_z}\mathsf{K}_{\mathrm{ff}}\mathsf{T}^{1}\boldsymbol{f}_1 + (\mathsf{M}_{\mathrm{ff}}^{N_z,+}\mathsf{T}^{N_z}\mathsf{K}_{\mathrm{fb}}\mathsf{T}^{N_z} + \mathsf{M}_{\mathrm{fb}}^{N_z,+})\boldsymbol{b}_{N_z} + \mathsf{R}_{\mathrm{fu}}^{N_z,+}\boldsymbol{u}_1 + \mathsf{R}_{\mathrm{fd}}^{N_z,+}\boldsymbol{d}_{N_x}\,, \\ \boldsymbol{b}_0 &= (\mathsf{M}_{\mathrm{bf}}^{0,-} + \mathsf{M}_{\mathrm{bb}}^{0,-}\mathsf{T}^{1}\mathsf{K}_{\mathrm{bf}}\mathsf{T}^{1})\boldsymbol{f}_1 + \mathsf{M}_{\mathrm{bb}}^{0,-}\mathsf{T}^{1}\mathsf{K}_{\mathrm{bb}}\mathsf{T}^{N_z}\boldsymbol{b}_{N_z} + \mathsf{R}_{\mathrm{bu}}^{0,-}\boldsymbol{u}_1 + \mathsf{R}_{\mathrm{bd}}^{0,-}\boldsymbol{d}_{N_x}\,, \\ \boldsymbol{u}_{N_x+1} &= \hat{\mathsf{R}}_{\mathrm{uf}}^{N_x,+}\boldsymbol{f}_1 + \hat{\mathsf{R}}_{\mathrm{ub}}^{N_x,+}\boldsymbol{b}_{N_z} + \hat{\mathsf{M}}_{\mathrm{uu}}^{N_x,+}\hat{\mathsf{T}}^{N_x}\hat{\mathsf{K}}_{\mathrm{uu}}\hat{\mathsf{T}}^{1})\boldsymbol{u}_1 + (\hat{\mathsf{M}}_{\mathrm{uu}}^{N_x,+}\hat{\mathsf{T}}^{N_x}\hat{\mathsf{K}}_{\mathrm{ud}}\hat{\mathsf{T}}^{N_x} + \hat{\mathsf{M}}_{\mathrm{ud}}^{N_x,+})\boldsymbol{d}_{N_x}\,, \\ \boldsymbol{d}_0 &= \hat{\mathsf{R}}_{\mathrm{df}}^{0,-}\boldsymbol{f}_1 + \hat{\mathsf{R}}_{\mathrm{db}}^{0,-}\boldsymbol{b}_{N_z} + (\hat{\mathsf{M}}_{\mathrm{du}}^{0,-} + \hat{\mathsf{M}}_{\mathrm{dd}}^{0,-}\hat{\mathsf{T}}^{1}\hat{\mathsf{K}}_{\mathrm{du}}\hat{\mathsf{T}}^{1})\boldsymbol{u}_1 + \hat{\mathsf{M}}_{\mathrm{dd}}^{0,-}\mathsf{T}^{1}\hat{\mathsf{K}}_{\mathrm{dd}}\hat{\mathsf{T}}^{N_x}\boldsymbol{d}_{N_x}\,, \end{aligned} \tag{40}$$

Substituting these expressions into the remaining four matrix equations results in the following linear system

$$\begin{pmatrix} \mathsf{X}_{\mathrm{ff}} & \mathsf{X}_{\mathrm{fb}} & \mathsf{X}_{\mathrm{fu}} & \mathsf{X}_{\mathrm{fd}} \\ \mathsf{X}_{\mathrm{bf}} & \mathsf{X}_{\mathrm{bb}} & \mathsf{X}_{\mathrm{bu}} & \mathsf{X}_{\mathrm{bd}} \\ \mathsf{X}_{\mathrm{uf}} & \mathsf{X}_{\mathrm{ub}} & \mathsf{X}_{\mathrm{uu}} & \mathsf{X}_{\mathrm{ud}} \\ \mathsf{X}_{\mathrm{df}} & \mathsf{X}_{\mathrm{db}} & \mathsf{X}_{\mathrm{du}} & \mathsf{X}_{\mathrm{dd}} \end{pmatrix} \begin{pmatrix} \boldsymbol{f}_1 \\ \boldsymbol{b}_{N_z} \\ \boldsymbol{u}_1 \\ \boldsymbol{d}_{N_x} \end{pmatrix} = \begin{pmatrix} \mathsf{M}_{\mathrm{ff}}^{0,+}\boldsymbol{f}_0 \\ \mathsf{M}_{\mathrm{bb}}^{N_z,-}\boldsymbol{b}_{N_z+1} \\ \hat{\mathsf{M}}_{\mathrm{uu}}^{0,+}\boldsymbol{u}_0 \\ \hat{\mathsf{M}}_{\mathrm{dd}}^{N_x,-}\boldsymbol{d}_{N_x+1} \end{pmatrix}, \tag{41}$$

with submatrices

$$
\begin{array}{ll}
\mathsf{X}_{\mathrm{ff}} = 1 - \mathsf{M}_{\mathrm{fb}}^{0,+}(\mathsf{M}_{\mathrm{bf}}^{0,-} + \mathsf{M}_{\mathrm{bb}}^{0,-}\mathsf{T}^1\mathsf{K}_{\mathrm{bf}}\mathsf{T}^1), & \mathsf{X}_{\mathrm{fb}} = -\mathsf{M}_{\mathrm{fb}}^{0,+}\mathsf{M}_{\mathrm{bb}}^{0,-}\mathsf{T}^1\mathsf{K}_{\mathrm{bb}}\mathsf{T}^{N_z}, \\
\mathsf{X}_{\mathrm{fu}} = \mathsf{R}_{\mathrm{fu}}^{0,+} - \mathsf{M}_{\mathrm{fb}}^{0,+}\mathsf{R}_{\mathrm{bu}}^{0,-}, & \mathsf{X}_{\mathrm{fd}} = \mathsf{R}_{\mathrm{fd}}^{0,+} - \mathsf{M}_{\mathrm{fb}}^{0,+}\mathsf{R}_{\mathrm{bd}}^{0,-}, \\
\mathsf{X}_{\mathrm{bf}} = -\mathsf{M}_{\mathrm{bf}}^{N_z,-}\mathsf{M}_{\mathrm{ff}}^{N_z,+}\mathsf{T}^{N_z}\mathsf{K}_{\mathrm{ff}}\mathsf{T}^1, & \mathsf{X}_{\mathrm{bb}} = 1 - \mathsf{M}_{\mathrm{bf}}^{N_z,-}(\mathsf{M}_{\mathrm{fb}}^{N_z,+} + \mathsf{M}_{\mathrm{ff}}^{N_z,+}\mathsf{T}^{N_z}\mathsf{K}_{\mathrm{fb}}\mathsf{T}^{N_z}), \\
\mathsf{X}_{\mathrm{bu}} = \mathsf{R}_{\mathrm{bu}}^{N_z,-} - \mathsf{M}_{\mathrm{bf}}^{N_z,-}\mathsf{R}_{\mathrm{fu}}^{N_z,+}, & \mathsf{X}_{\mathrm{bd}} = \mathsf{R}_{\mathrm{bd}}^{N_z,-} - \mathsf{M}_{\mathrm{bf}}^{N_z,-}\mathsf{R}_{\mathrm{fd}}^{N_z,+}, \\
\mathsf{X}_{\mathrm{uf}} = \hat{\mathsf{R}}_{\mathrm{uf}}^{0,+} - \hat{\mathsf{M}}_{\mathrm{ud}}^{0,+}\hat{\mathsf{R}}_{\mathrm{df}}^{0,-}, & \mathsf{X}_{\mathrm{ub}} = \hat{\mathsf{R}}_{\mathrm{ub}}^{0,+} - \hat{\mathsf{M}}_{\mathrm{ud}}^{0,+}\hat{\mathsf{R}}_{\mathrm{db}}^{0,-}, \\
\mathsf{X}_{\mathrm{uu}} = 1 - \hat{\mathsf{M}}_{\mathrm{ud}}^{0,+}(\hat{\mathsf{M}}_{\mathrm{du}}^{0,-} + \hat{\mathsf{M}}_{\mathrm{dd}}^{0,-}\hat{\mathsf{T}}^1\hat{\mathsf{K}}_{\mathrm{du}}\hat{\mathsf{T}}^1), & \mathsf{X}_{\mathrm{ud}} = -\hat{\mathsf{M}}_{\mathrm{ud}}^{0,+}\hat{\mathsf{M}}_{\mathrm{dd}}^{0,-}\hat{\mathsf{T}}^1\hat{\mathsf{K}}_{\mathrm{dd}}\hat{\mathsf{T}}^{N_x}, \\
\mathsf{X}_{\mathrm{df}} = \hat{\mathsf{R}}_{\mathrm{df}}^{N_x,-} - \hat{\mathsf{M}}_{\mathrm{du}}^{N_x,-}\hat{\mathsf{R}}_{\mathrm{uf}}^{N_x,+}, & \mathsf{X}_{\mathrm{db}} = \hat{\mathsf{R}}_{\mathrm{db}}^{N_x,-} - \hat{\mathsf{M}}_{\mathrm{du}}^{N_x,-}\hat{\mathsf{R}}_{\mathrm{ub}}^{N_x,+}, \\
\mathsf{X}_{\mathrm{du}} = -\hat{\mathsf{M}}_{\mathrm{du}}^{N_x,-}\hat{\mathsf{M}}_{\mathrm{uu}}^{N_x,+}\hat{\mathsf{T}}^{N_x}\hat{\mathsf{K}}_{\mathrm{uu}}\hat{\mathsf{T}}^1, & \mathsf{X}_{\mathrm{dd}} = 1 - \hat{\mathsf{M}}_{\mathrm{du}}^{N_x,-}(\hat{\mathsf{M}}_{\mathrm{ud}}^{N_x,+} + \hat{\mathsf{M}}_{\mathrm{uu}}^{N_x,+}\hat{\mathsf{T}}^{N_x}\hat{\mathsf{K}}_{\mathrm{ud}}\hat{\mathsf{T}}^{N_x}),
\end{array}
\tag{42}
$$

where the given coefficients $\boldsymbol{f}_0$, $\boldsymbol{b}_{N_z+1}$, $\boldsymbol{u}_0$, $\boldsymbol{d}_{N_x+1}$ of the incoming waves on the external regions form the right hand side. Via Eqs. (22), (23), and (40), a solution of Eq. (41) determines all unknown coefficients in the expansion (3), i.e. solves the scattering problem.

3 Numerical examples

While a detailed study of convergence properties of the QUEP scheme remains beyond the scope of this paper, we give a few remarks on observations during the practical execution of the simulations.

The scheme has been implemented using the object-oriented features of the C++ language, as close as possible along the abstract formulation of Section 2. The implementation rests on a mode solver for multilayer dielectric slab waveguides. For the present lossless structures, the basis fields can be restricted to profiles with real transverse components, and either purely real or purely imaginary propagation constants. The internal mode representation as well as the computation of overlap integrals is kept as far as possible on an analytical level.

The mode solver engine relies on a search algorithm along the real axis of squared propagation constants, driven by the nodal properties of the basis modes. The routines have to work reliably for rather nonstandard refractive index profiles, that emerge from the alternative horizontal and vertical viewpoints. Where applicable, symmetry properties are exploited to resolve mode degeneracies. In a few instances, permittivity profiles become relevant that consist of individual regions with high refractive index, separated by a relatively large low index gap (examples are the central vertical segment and the central horizontal layer in the photonic crystal structure of Section 3.5). For the lowest order modes with exponential shapes in the intermediate low index region, the high index parts are numerically decoupled. The mode solver treats these cases accordingly: Up to a suitable limit of effective index, the lowest order basis fields are determined separately for the decoupled regions, and then joined with the higher oder modes computed on the entire interval to form the full expansion basis.

The QUEP algorithm turns out to be quite robust in general, where the quality of the approximation is determined by the number of expansion terms used, and by the extension of the computational window. Values for these parameters are given for the specific examples in Sections 3.1–3.5. So far the choice of the window boundaries x_0, x_{N_x}, z_0, z_{N_z} is a matter of intuition (and of tests on the stability of specific results versus the boundary positions), where the extension of the guided modes in the problem can give an orientation. In the limit of infinite expansions, the completeness properties of the basis mode sets guarantee in principle a perfect matching of the fields at the horizontal and vertical interfaces. For a finite set of basis modes the adjacent fields can match more or less adequately, depending on the structure under consideration. Apart from an erroneously discontinuous field, an insufficient number of expansion terms usually shows up by a violation of power conservation.

Occasionally, when computing series of varying configurations using fixed settings for the computational window and the number of basis modes, singular instabilities (i.e. few values off an otherwise straight line) were observed. If magnified, these instabilities exhibit a resonant-like behaviour, with respect to more or less all structural and computational parameters. We did not perceive a correlation with singular basis mode properties, e.g. a mode approaching a cut-off configuration. The phenomenon appears to be more pronounced for simulations of TM polarized light, where the electric field components are known to exhibit sharp singularities

around dielectric corners [25, 26]. Drastically increasing the number of expansion terms leads again to regular results, at the cost of a high computational effort, which does not seem to be adequate when comparing with neighboring configurations in a series of simulations.

Fortunately, the singular instances are always accompanied by pronounced errors in the power in- and outflow balance. Hence, although the precise origin of the instabilities remains unclear, we could apply the following practical approach to regularize the computations. The computational window should ideally not influence the results at all, apart from the corner points; this in fact holds reasonably well in case of the regular configurations. Nevertheless, the shape of the nonguided basis modes is dominated by the position of the window boundaries. A particular mismatch of basis mode sets in case of a singular configuration can thus be altered effectively by shifting x_0, x_{N_x}, z_0, z_{N_z}, and here one observes indeed a strong influence of these positions. Therefore, a solution of Eqs. (41) is accepted, if the ratio of the total input and output power is calculated within a narrow interval around 1 (uniform limits e.g. used for the waveguide crossings in Section 3.3 (TM) are $[0.995, 1.002]$). Otherwise simulations of the same structure with slightly shifted window boundaries (displacement for Section 3.3, TM: subsequently $0.05\,\mu$m, $0.1\,\mu$m, $0.2\,\mu$m) are substituted until the power conservation criterion is satisfied. This strategy leads to the more or less smooth results as shown in Sections 3.1–3.5.

The computational effort of a QUEP simulation is roughly comparable to two times a BEP simulation of the structure under investigation, where first the sequence of inner vertical slices, second the sequence of inner horizontal layers is considered. This corresponds to the procedure that leads to Eqs. (22) and (23). Additionally, the system (41) is to be analyzed once. Hence the largest matrix for which a linear system of equations is to be solved is of a size $(M_1^x + M_{N_z}^x + M_1^z + M_{N_x}^z) \times (M_1^x + M_{N_z}^x + M_1^z + M_{N_x}^z)$, or of a size $(2M_x + 2M_z) \times (2M_x + 2M_z)$ in a setting with uniform expansion terms $M_s^x = M_x$ and $M_l^z = M_z$, i.e. of about four times the dimension of the matrices that are to be inverted in the inner BEPs. Note that the BEP parts of the procedure could be regarded as a way to solve systems of linear equations for $2(N_z + 1)M_x$ unknowns in the slice decomposition, or for $2(N_x + 1)M_z$ unknowns in the layer decomposition. In total these are systems (though with a specific block structure) far larger than the dimension of (41). Obviously the effort depends crucially on the numbers N_z and N_x of slices and layers; the solution of Eq. (41) does not dominate the operation count.

3.1 Gaussian beams in free space

Wave propagation in free space is selected as a first, most simple test. Figure 2 illustrates field profiles as predicted by the QUEP algorithm, for Gaussian beams excited on arbitrary sides of the inner computational window. The field is discretized by $M_x = M_z = 150$ Fourier components along both coordinate axes, on a window of $[0, 15.1]\,\mu\text{m} \times [0, 15.1]\,\mu\text{m}$. Apart from the inner rectangle, the plots include parts of the external regions as well; the wedges at the corners indicate the outer Dirichlet boundaries.

Inset (a) shows a beam traversing the computational window along the z-axis, and the corresponding spreading of the Gaussian profile. This is what can be expected from a conventional BEP implementation. According to (b) and (c), here beams can be launched along the vertical x-axis as well, or simultaneously from all four sides; the two axes are treated alike. For parts (d), (e), and (f), beams are launched on one of the vertical sides under a higher angle, such that they leave the window via one of the horizontal sides. With the QUEP approach fully transparent boundary conditions are realized, that allow for simultaneous influx and outflux along the four edges of the inner computational window.

Similar calculations should be possible with a conventional BEP scheme as well, if suitably adjusted transparent boundary conditions (typically perfectly matched layers, see e.g. [14]) are included. This would require to rotate the simulation setting by 90° (b,c), to employ a formulation with double sided influx (c, f), and to superimpose four (one sided influx) or two (double sided influx) separate simulations for computing the interference patterns in (c). Note that such a superposition approach would be considerably more difficult if guided wave influx and outflux along more than one coordinate axis is to be modeled, as in the examples of Sections 3.3–3.5.

The field plots show only minor influence of the corner points, where the basis components E_y (TE) or H_y (TM) are enforced to be zero. Waves with cylindrical shape are visible, originating from these points, with major amplitudes in the external regions $x, z < 0$ or $x, z > 15.1\,\mu$m that do not belong to the actual computational window. Within the present formulation, the remnant small perturbations inside the window can only be suppressed by enlarging the computational domain, or by modifying the position or aspect ratio of the window.

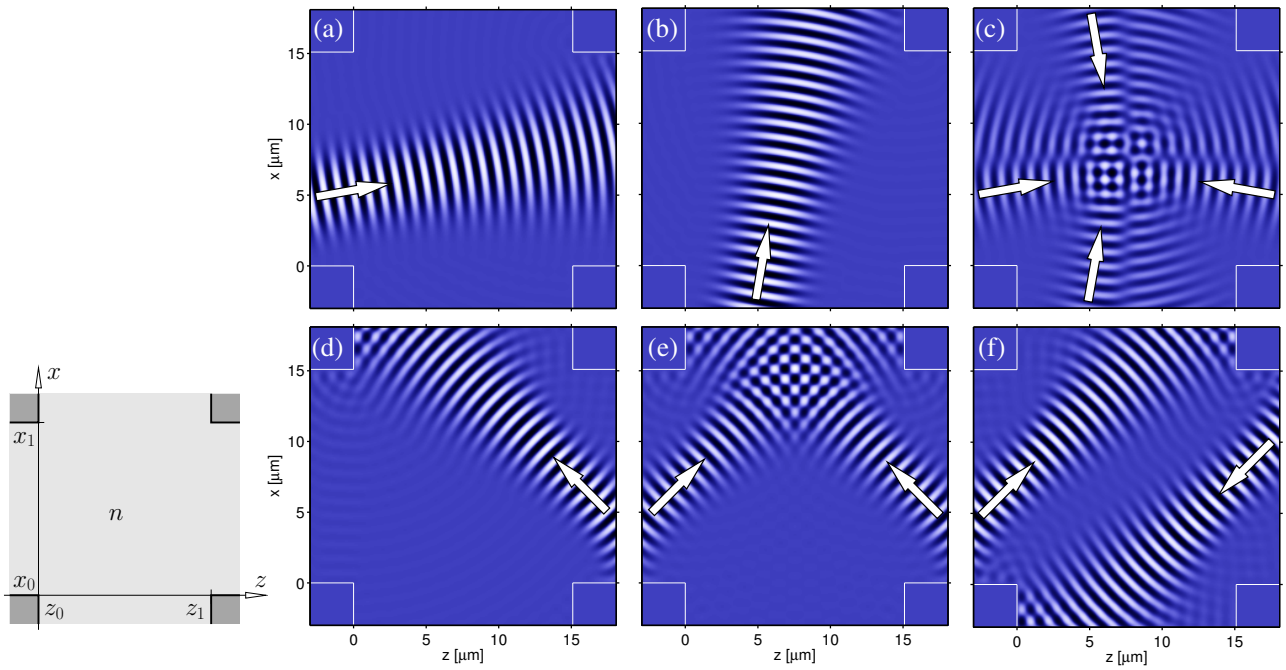

Figure 2: Propagation of Gaussian beams, TE waves ($\lambda = 1\,\mu$m) in a homogeneous medium, $n = 1.0$. The plots show snapshots of the optical electric field profile E_y. (a) – (c): Beams (width $4\,\mu$m, tilt angle $10°$, offset $2\,\mu$m with respect to the center of the window) are launched from the left and bottom edges, and simultaneously from all four edges. (d) – (f): Centered beams, now with a tilt angle of $45°$, are launched such that the rays leave the computational window across the upper and lower horizontal edges, while they are excited on the left and right edges of the domain.

3.2 Waveguide Bragg gratings

As an example for a more involved structure where transparent boundaries are essential, we consider a waveguide-Bragg-grating with varying etching depth, used as a benchmark problem to compare different modeling tools in Ref. [27]. Figure 3 introduces the geometry.

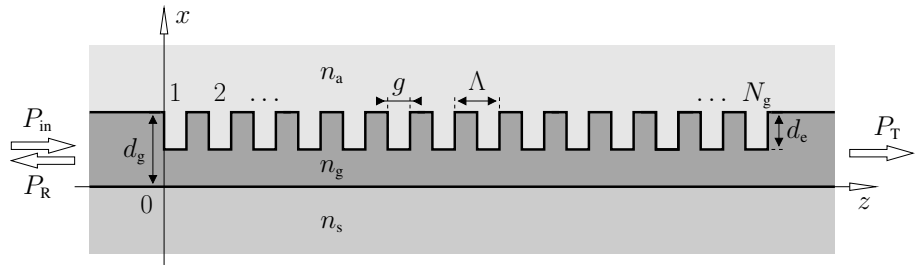

Figure 3: A waveguide-Bragg-grating, benchmark problem from Ref. [27]. $N_g = 20$ grooves of width $g = \Lambda/2$ and depth d_e are etched into a slab of thickness $d_g = 0.5\,\mu$m, with a period $\Lambda = 0.430\,\mu$m. $n_s \approx 1.45$, $n_g \approx 1.99$, and $n_a = 1.0$ are the refractive indices of the substrate, film, and cover layers.

The grating is excited by the guided, TE polarized mode of the outer slab waveguide; interest is in the relative guided transmitted and reflected power fractions. The benchmark requires to incorporate the realistic wavelength dispersion of the core material, according to a recipe as detailed in Ref. [27]. The dispersion is included in all computations underlying the curves of Figure 4, where, on the scale of the figure, only very minor differences to results for $n_s = 1.45$, $n_g = 1.99$ appear. All QUEP results are obtained with a computational window $[z_0, z_{41}] \times [x_0, x_{4,5}] = [-1.8, 10.185]\,\mu\text{m} \times [-4, 2]\,\mu\text{m}$, discretized uniformly by $M_z = 120$ and $M_x = 60$ basis functions.

The curves labeled "BEP, PML b.c." correspond to the BEP2 results of Ref. [27], computed by means of a bidirectional eigenmode propagation algorithm [28, 7] with perfectly matched layer boundary conditions [29, 30]. The comparison to other, entirely different approaches in Ref. [27] gives some confidence that these results can serve as a reliable reference. One observes an excellent agreement with the QUEP results. In contrast to the reference BEP, the periodicity of the grating is not exploited in the QUEP formalism. Therefore

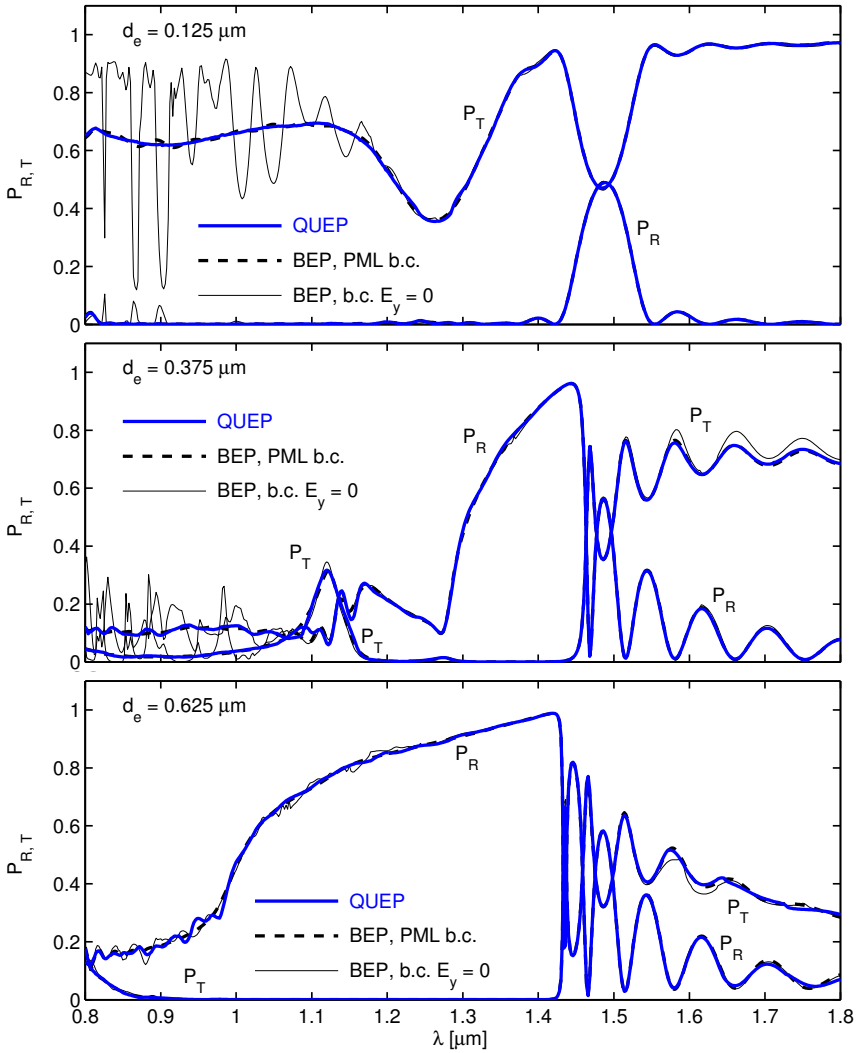

Figure 4: Spectral response of waveguide Bragg gratings according to the specification of Figure 3. The plots show the relative guided transmission P_T and reflection P_R as a function of the vacuum wavelength λ, for three different etching depths d_e. Bold continuous lines indicate power levels as predicted by the present method. The thin continuous lines are results of a conventional BEP technique, with Dirichlet boundary conditions. Bold dashed lines correspond to reference data from Ref. [27], computed by means of a BEP algorithm with PML boundary conditions.

the computation times are not comparable; the present QUEP algorithm is certainly not a method of choice in case of piecewise periodic configurations, where a simulation could make use of the Bloch- or Floquet-theorem.

For comparison, Figure 4 includes also curves for BEP computations with basis fields defined by Dirichlet boundary conditions (actually half of the QUEP basis fields), on the same rather narrow vertical window $x \in [-4, 2]\,\mu$m as used for the QUEP simulation. While one finds a more or less satisfying agreement with the more sophisticated approaches in the long wavelength regions, for shorter wavelengths the behaviour of the "Dirichlet BEP" becomes entirely irregular. The results in this wavelength region depend strongly on the boundary positions, indicating that reflections from these boundaries disturb the computations around the corrugated waveguide core. Obviously these reflections can be suppressed effectually by means of the additional vertical eigenmode expansion in the QUEP approach.

3.3 Waveguide crossings

Structures with guided wave input and output along both relevant coordinate axes are most interesting in the present context. Figure 5 shows results for a series of waveguide crossings with varying width of the vertical core. Light with fixed vacuum wavelength is launched via the fundamental, alternatively TE or TM polarized mode of the horizontal waveguide. The plots show only the guided parts of the outgoing power fractions. The QUEP simulations use uniformly $M_x \times M_z = 120 \times 120$ expansion terms on a symmetric $6\,\mu\text{m} \times 6\,\mu\text{m}$ computational window. In particular for the TM computations in this example, the regularization technique as discussed at the beginning of Section 3 had to be applied.

As it is to be expected for the high refractive index contrast waveguides, the simulations yield quite different transmission characteristics for TE and TM polarized light. Concerning the losses and the guided power scattered into the vertical waveguide, the intersection has a much stronger influence on the TE waves than on TM

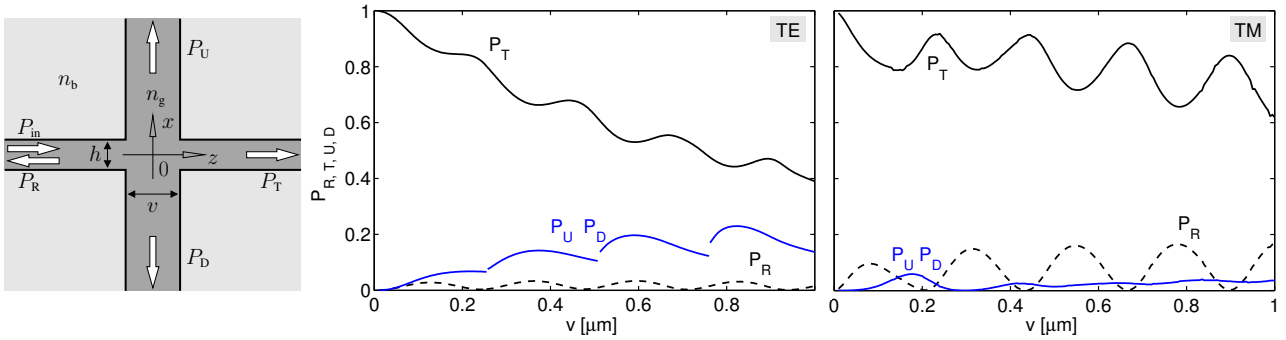

Figure 5: Simulations of waveguide crossings, dependence of the relative guided powers P_R, P_T, P_U, P_D, that are reflected, transmitted, and upwards and downwards scattered, respectively, on the width v of the vertical core, for TE polarization (left), TM polarization (right), and a vacuum wavelength of $\lambda = 1.55\,\mu$m. The horizontal guide (thickness $h = 0.2\,\mu$m, refractive indices $n_b = 1.45$ (background) and $n_g = 3.40$ (core)) is intersected by a vertical waveguide of variable width.

polarized light, while the guided reflections are more pronounced for TM polarization than for TE light.

Perhaps the difference in the strength of the vertical scattering could be explained by imagining a properly polarized oscillating dipole at the exit $(x = 0, z = -v/2)$ of the left half of the horizontal core. While its radiation covers both the x- and z-directions in the TE case, for TM polarization the (2D) radiation is oriented more or less along the z-axis. Hence only minor power fractions of TM light are guided upwards and downwards.

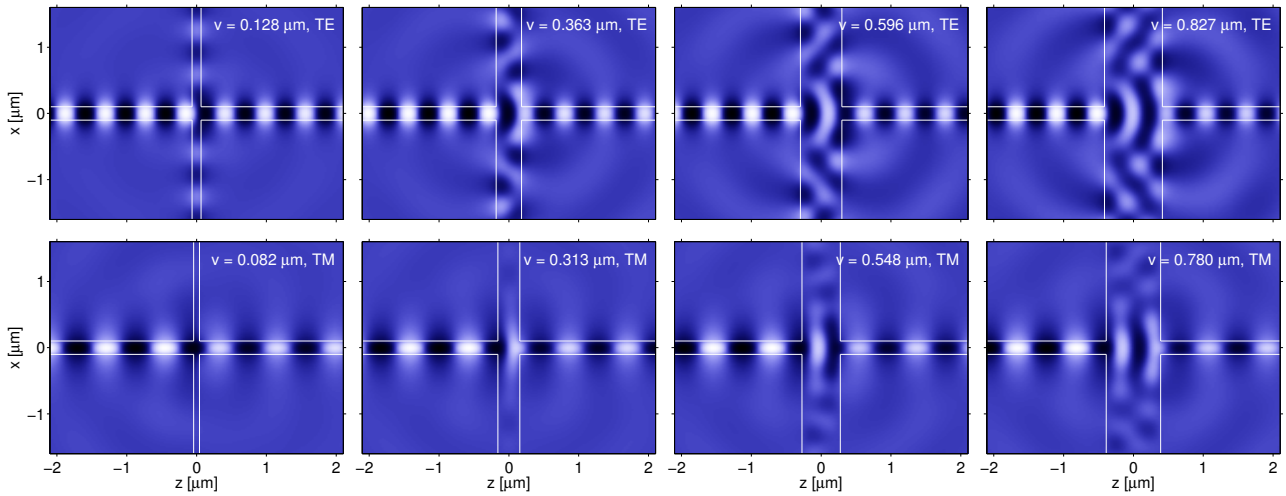

Figure 6: Light propagation through the waveguides crossings of Figure 5, snapshots of the optical electric field E_y (TE, top row) or of the basic magnetic field component H_y (TM, bottom row), for different widths v of the vertical core.

One observes an oscillatory behaviour of all curves in Figure 5. For a series of configurations with maximum guided reflection, Figure 6 collects snapshots of the basis field components, evaluated at times where the partly standing waves in the input waveguide are at extremal levels. Apparently the oscillations correspond to the growing number of guided modes that are supported by the vertical core: At least for the TE polarized fields one can identify the nodal lines of the vertically propagating modes, although the actual field will be the beating pattern of a mode superposition. With growing v, the vertically traveling fields that eventually become guided TE modes (propagating, non evanescent fields with effective indices below the background level n_b) carry some power even below cut-off. Therefore one observes the discontinuities in the curves for P_D and P_U at the widths v where the wave is actually counted as a guided mode. This is obviously not the case for TM polarization.

Widths v with vanishing reflection are present for both polarizations. Probably the almost periodic oscillation of P_R with v can be interpreted as a Fabry-Perot effect of the transition across the vertical core: Apart from sign changes one observes very similar field patterns (e.g. distances of the first maximum / minimum from the junctions) in the horizontal input and exit waveguide segments. For the extremal configurations of Figure 6, integer multiples of half wavelengths inside the vertical intersection match the same field extensions in the left and right parts of the horizontal core.

3.4 Square resonator with perpendicular ports

A square microresonator as investigated in [31, 13] serves as an example how the present approach can adequately capture resonance phenomena. We consider a cavity constructed on the basis of a slab mode viewpoint as outlined in [32], here a three port configuration with two perpendicular bus waveguides according to the sketch of Figure 7. The cavity is excited via the fundamental, right traveling mode of the lower waveguide. Interest is in the wavelength dependence of the guided power transfer. The QUEP results in Figure 7 are obtained uniformly with 100×100 expansion terms on a computational window $[-4, 4]\,\mu\text{m} \times [-4, 4]\,\mu\text{m}$.

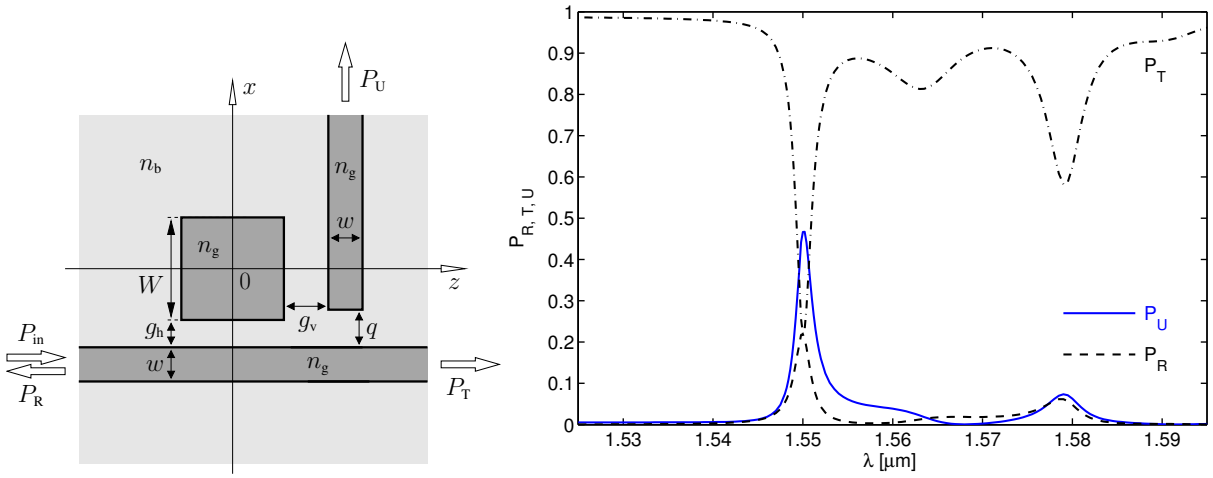

Figure 7: Spectral power transmission through a square resonator with perpendicularly oriented port waveguides. A cavity of width and height $W = 1.786\,\mu$m couples the two identical cores with a thickness $w = 0.1\,\mu$m. Refractive indices of $n_g = 3.4$ and $n_b = 1.0$ were assumed for the guiding regions and the background, respectively. The horizontal and vertical gaps are $g_h = 0.355\,\mu$m and $g_v = 0.385\,\mu$m; the vertical waveguide ends $q = 0.355\,\mu$m away from the horizontal core. The curves indicate the relative levels of reflected, transmitted, and upwards scattered guided power P_R, P_T, P_U as a function of the vacuum wavelength λ, for TE polarized input light.

Off-resonance, most of the input light just passes along the square cavity. In case of a resonance, apart from losses to radiation the cavity scatters major parts of the input power into the three output ports. For the pronounced resonance at $\lambda = 1.55\,\mu$m, an almost ideal configuration is realized with a quarter reflection, a quarter transmission, and with half the input power scattered into the vertical bus waveguide.

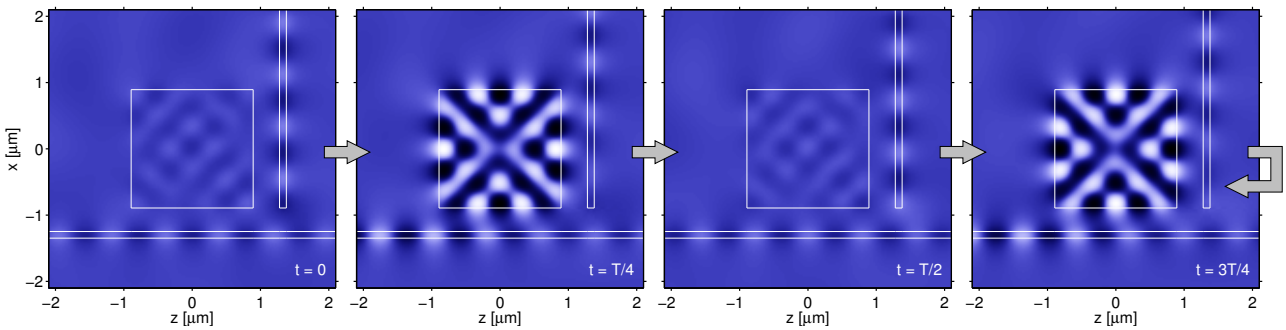

Figure 8: Light propagation through the resonator configuration of Figure 7 at the resonance wavelength $\lambda = 1.55\,\mu$m. The plots show snapshots of the TE field component E_y, at four times t that are equidistantly distributed over one time period $T = 5.17$ fs. The simulation predicts levels of $P_R = 22\%$, $P_T = 22\%$, and $P_U = 46\%$ for the outgoing relative guided power.

Figure 8 illustrates field pattern that accompanies the resonance. One observes outgoing traveling waves in the upper and lower right ports, a partly standing and partly traveling wave in the lower left input port. Inside the square cavity a typical standing wave pattern establishes, here a high-quality bimodal resonance, made up of the 4th and 6th order TE modes of a symmetric slab of thickness W, with refractive index contrast n_g/n_b at the design wavelength $\lambda = 1.55\,\mu$m. The second resonance at $\lambda = 1.579\,\mu$m corresponds to a single mode excitation based on the 5th order slab mode, with much lower quality. Details on these constructions can be found in Ref. [32].

3.5 Photonic crystal bend

A 90 degree bend of a 2D photonic crystal waveguide constitutes the last, most involved example. We adopted a "classical" parameter set as introduced in [33, 2]. Figure 9 sketches the configuration and shows the spectral transmission and reflection of the bend. The simulation includes the transition to conventional input- and output waveguides, according to an optimization in [34]. While on the one hand this seems to be quite adequate for a realistic simulation, it also emphasizes a restriction of the present modeling scheme: The exterior regions need to be homogeneous along the respective coordinate axes; half infinite periodic permittivity profiles as required for a simulation of the isolated photonic crystal bend without transitions can not be represented by the expansions (3).

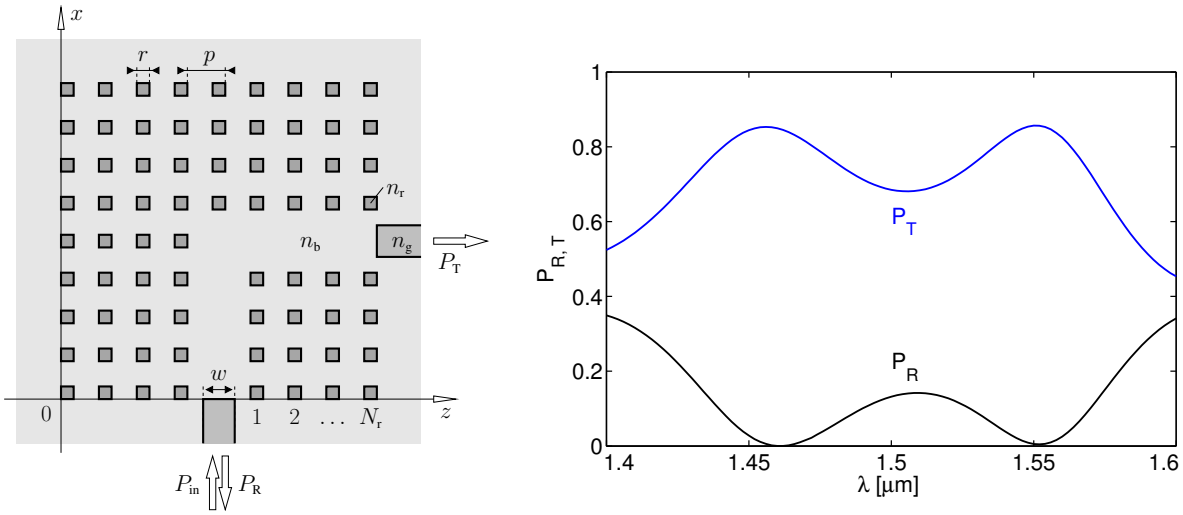

Figure 9: Spectral response of a photonic crystal bend according to a specification of Refs. [33, 2]: square silicon rods ($n_r = 3.4$) of width $0.150\,\mu$m in air ($n_b = 1.0$), arranged in a square lattice with period $p = 0.6\,\mu$m and $N_r = 4$ rows of rods in the reflector regions around the photonic crystal channel. The simulations include the transitions to conventional guiding cores of width $w = 0.5\,\mu$m and refractive index $n_g = 1.8$. P_R and P_T are the relative guided power fractions that are reflected and transmitted through the bend.

The QUEP simulations use $M_x = M_z = 120$ expansion terms on each slice / layer, on a computational window $[-1.2, 6.15]\,\mu\text{m} \times [-1.2, 6.15]\,\mu\text{m}$. For this structure establishing the basis mode sets for the various 1D refractive index profiles turns out to be more involved, i.e. the approaches mentioned in the beginning of Section 3 are required. Symmetry properties allow to separate nearly degenerate modes in the slices/layers with the inner periodic rod/air pattern. The decoupling strategy can be applied to the central vertical segment (and the central horizontal layer), consisting of the upper grating region, and the lower external core part, separated by a wide low index region.

Originally the conventional port waveguides were shaped for low losses at the transition to the photonic crystal waveguides [34], at a wavelength of $\lambda = 1.5\,\mu$m. The present simulations of the full structure, however, predict transmission maxima with almost vanishing reflection at two quite different wavelengths. The corresponding field pattern in Figure 10 show partly standing waves along the line of missing rods in the photonic crystal region, with 2 wavelengths ($\lambda = 1.551\,\mu$m) or 2.5 wavelengths ($\lambda = 1.461\,\mu$m) fitting between the two junctions. Apparently the transmission maxima can be understood as Fabry-Perot resonances in the photonic crystal channel, established by the transitions between the photonic crystal waveguide and the external conventional cores.

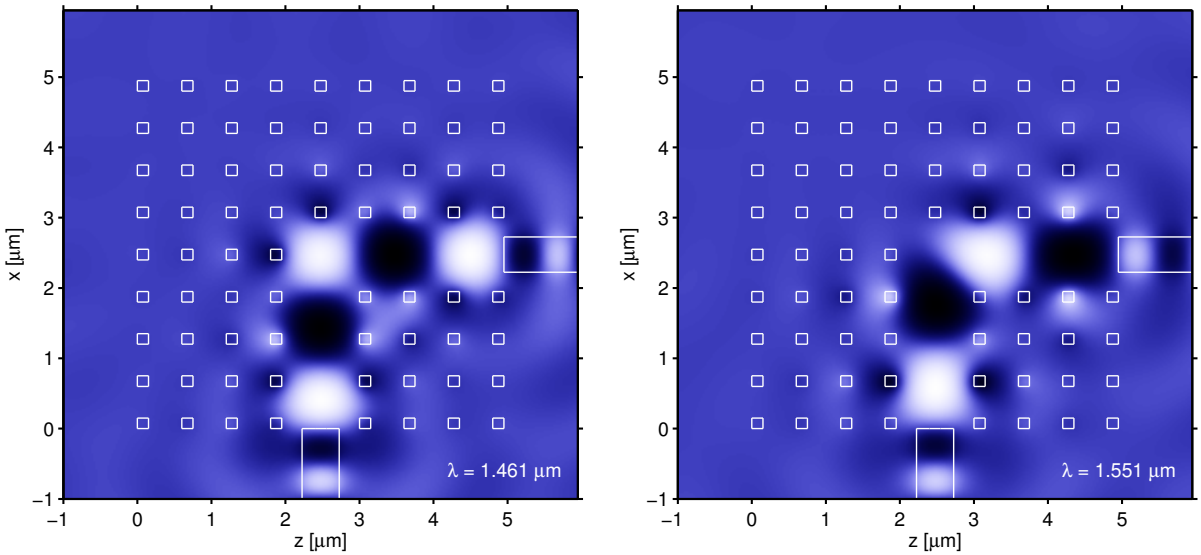

Figure 10: Light propagation along the photonic crystal bend as introduced in Figure 9, snapshots of the electric field component E_y of the TE fields, for extremal configurations of the field in the photonic crystal region. The vacuum wavelengths $\lambda = 1.461$ μm (left) and $\lambda = 1.551$ μm (right) correspond to the transmission maxima / reflection minima in Figure 9.

4 Concluding remarks

A simulation technique for problems of fixed-frequency wave propagation in integrated optics has been discussed, intended for 2D structures with piecewise constant, rectangular, so far lossless refractive index profiles. With the rigorous expansion of the optical electromagnetic field into eigenmodes that propagate along two perpendicular coordinate axes, one can view the fields generated by the QUEP technique as a superposition of two fields obtained by suitably connected, perpendicularly oriented BEP simulations.

The quadridirectional mode expansion provides a completely equivalent treatment of the wave propagation along the two relevant axes. One can view the approach as a way to realize transparent boundaries for the rectangular central region on an unbounded, cross-shaped computational domain. Modeling simultaneous guided and nonguided influx and outflux over all four boundaries is straightforward; the computational effort remains moderate. While preserving the advantages (accuracy, efficiency, interpretability) of the BEP tools, the proposed technique is capable to adequately capture the phenomena related to omnidirectional 2D light propagation.

Certainly different formulations of the present algorithm are possible. At least for the TE case, the scattering problem is governed by a standard scalar Helmholtz equation. The products (1) and (2) can be replaced by common L_2-inner products, with integrations along either the x- or z-directions. Then the projection on inwards and outwards propagating fields, leading e.g. to Eqs. (12) and (24), becomes equivalent to the L_2-projection of equalities for the scalar field itself, and for the derivative of the field along the direction perpendicular to the respective interfaces. The subsequent algebraic procedure should be more or less the identical. However, the formulation given in Section 2 is based on well established, more physical notions, and covers both the TE and TM cases.

Naturally, when compared to methods based on rigorous spatial discretizations, the present quasi-analytical approach is applicable only to a smaller range of problems. Nevertheless, within these limits the method permits sufficient flexibility to study systems that are of interest in the current integrated optics research, as demonstrated by the examples in Section 3.

Acknowledgments

The author would like to thank E. van Groesen, H. J. W. M. Hoekstra, R. Stoffer, and R. Pregla for many fruitful discussions on the subject. J. Čtyroký kindly provided the reference data sets on Bragg gratings for Figure 4.

References

[1] M. Bertolotti, A. Driessen, and F. Michelotti, editors. *Microresonators as building blocks for VLSI photonics*. AIP conference proceedings, Melville, New York, to appear 2004. Proceedings of the International School of Quantum Electronics, 39th course, Erice, Sicily.

[2] J. D. Joannopoulos, R. D. Meade, and J. N. Winn. *Photonic Crystals: Molding the Flow of Light*. Princeton, 1995.

[3] H. J. W. M. Hoekstra. On beam propagation methods for modelling in integrated optics. *Optical and Quantum Electronics*, 29:157–171, 1997.

[4] A. Taflove and S. C. Hagness. *Computational Electrodynamis: The Finite Difference Time Domain Method, 2nd ed.* Artech House, Norwood, MA, USA, 2000.

[5] F. Schmidt. Computation of discrete transparent boundary conditions for the 2D Helmholtz equation. *Optical and Quantum Electronics*, 30(5/6):427–441, 1998.

[6] C. Vassallo. *Optical Waveguide Concepts*. Elsevier, Amsterdam, 1991.

[7] G. Sztefka and H. P. Nolting. Bidirectional eigenmode propagation for large refractive index steps. *IEEE Photonics Technology Letters*, 5(5):554–557, 1993.

[8] J. Willems, J. Haes, and R. Baets. The bidirectional mode expansion method for two-dimensional waveguides: the TM case. *Optical and Quantum Electronics*, 27:995–1007, 1995.

[9] P. Bienstmann, L. Vanholme, and R. Baets. CAMFR — CAvity Modelling FRamework. http://camfr.sourceforge.net/ .

[10] FIMMPROP — A bidirectional optical propagation tool. Photon Design, 34 Leopold Street, Oxford OX4 1TW, United Kingdom; http://www.photond.com/ .

[11] OlympIOs Integrated Optics Software. C2V, P.O. Box 318, 7500 AH Enschede, The Netherlands; http://www.c2v.nl/software/ .

[12] M. Lohmeyer and R. Stoffer. Integrated optical cross strip polarizer concept. *Optical and Quantum Electronics*, 33(4/5):413–431, 2001.

[13] M. Lohmeyer. Mode expansion modeling of rectangular integrated optical microresonators. *Optical and Quantum Electronics*, 34(5):541–557, 2002.

[14] P. Bienstmann and R. Baets. Advanced boundary conditions for eigenmode expansion models. *Optical and Quantum Electronics*, 34(5/6):523–540, 2002.

[15] E. Kühn. A mode-matching method for solving field problems in waveguide and resonator circuits. *AEÜ International Journal of Electronics and Communication*, 27:511–518, 1973.

[16] F. Arndt, I. Ahrens, U. Papziner, U. Wiechmann, and R. Wilkeit. Optimized E-plane T-junction series power dividers. *IEEE Transactions on Microwave Theory and Techniques*, MTT-35(11):1052–1059, 1987.

[17] F. Alessandri, M. Mongiardo, and R. Sorrentino. A technique for the fullwave automatic synthesis of waveguide components: Application to fixed phase shifters. *IEEE Transactions on Microwave Theory and Techniques*, 40(7):1484–1495, 1992.

[18] J. Rebollar, J. Esteban, and J. E. Page. Fullwave analysis of three and four-port rectangular waveguide junctions. *IEEE Transactions on Microwave Theory and Techniques*, 42(2):256–263, 1994.

[19] W. Pascher and P. Pregla. Analysis of rectangular waveguide discontinuities by the method of lines. *IEEE Transactions on Microwave Theory and Techniques*, 43(2):416–420, 1995.

[20] W. Pascher and P. Pregla. Analysis of rectangular waveguide junctions by the method of lines. *IEEE Transactions on Microwave Theory and Techniques*, 43(12):2649–2653, 1995.

[21] P. Pregla. The analysis of general axially symmetric antennas with a coaxial feed line by the method of lines. *IEEE Transactions on Antennas and Propagation*, 46(10):1433–1443, 1998.

[22] R. Pregla. MoL-analysis of rectangular waveguide junctions by an impedance/admittance transfer concept and crossed discretization lines. *AEÜ International Journal of Electronics and Communication*, 53(2):83–91, 1999.

[23] L. A. Greda and R. Pregla. Analysis of coplanar T-junctions by the method of lines. *AEÜ International Journal of Electronics and Communication*, 55(5):313–318, 2001.

[24] P. Pregla. Efficient and accurate modeling of planar anisotropic microwave structures by the method of lines. *IEEE Transactions on Microwave Theory and Techniques*, 50(06):1469–1479, 2002.

[25] A. S. Sudbø. Why are accurate computations of mode fields in rectangular dielectric waveguides difficult? *Journal of Lightwave Technology*, 10(4):418–419, 1992.

[26] M. Bressan and P. Gamba. Analytical expressions of field singularities at the edge of four right wedges. *IEEE Microwave and Guided Wave Letters*, 4(1):3–5, 1994.

[27] J. Čtyroký, S. Helfert, R. Pregla, P. Bienstmann, R. Baets, R. de Ridder, R. Stoffer, G. Klaase, J. Petráček, P. Lalanne, J.-P. Hugonin, and R. M. De La Rue. Bragg waveguide grating as a 1D photonic band gap structure: Cost 268 modelling task. *Optical and Quantum Electronics*, 34(5/6):455–470, 2002.

[28] J. Čtyroký, S. Helfert, and R. Pregla. Analysis of a deep waveguide Bragg grating. *Optical and Quantum Electronics*, 30(5/6):343–358, 1998.

[29] J. P. Bérenger. A perfectly matched layer for the absorption of electromagnetic waves. *Journal of Computational Physics*, 114(2):185–200, 1994.

[30] W. C. Chew, J. M. Jin, and E. Michielssen. Complex coordinate stretching as a generalized absorbing boundary condition. *Microwave and Optical Technology Letters*, 15(6):363–369, 1997.

[31] C. Manolatou, M. J. Khan, S. Fan, P. R. Villeneuve, H. A. Haus, and J. D. Joannopoulos. Coupling of modes analysis of resonant channel add-drop filters. *IEEE Journal of Quantum Electronics*, 35(9):1322–1331, 1999.

[32] M. Hammer. Resonant coupling of dielectric optical waveguides via rectangular microcavities: The coupled guided mode perspective. *Optics Communications*, 214(1–6):155–170, 2002.

[33] R. Stoffer, H. J. W. M. Hoekstra, R. M. de Ridder, E. van Groesen, and F. P. H. van Beckum. Numerical studies of 2D photonic crystals: Waveguides, coupling between waveguides and filters. *Optical and Quantum Electronics*, 32:947–961, 2000.

[34] R. Stoffer. *Uni- and Omnidirectional Simulation Tools for Integrated Optics*. University of Twente, Enschede, The Netherlands, 2001. Ph.D. Thesis.